Applied Geochemistry 102 (2019) 171–185

Contents lists available at ScienceDirect

Applied Geochemistry

journal homepage: www.elsevier.com/locate/apgeochem

# Induced geochemical reactions by compressed air energy storage in a porous formation in the North German Basin

Bo Wang*, Sebastian Bauer

*Institute of Geosciences, University of Kiel, Germany*

ARTICLE INFO

Editorial handling by Dr T Pichler

*Keywords:*
Compressed air energy storage
Geological porous formations
Induced geochemical reactions

ABSTRACT

A synthetic diabatic compressed air energy storage (CAES) based on an existing surface facility and using the Rhaetian sandstone formation in the North German Basin as porous storage reservoir is investigated for induced geochemical reactions. A daily storage cycle with a 6-h injection and a 6-h extraction phase in the early morning and late afternoon is applied. The chosen mineral assemblage shows the presence of pyrite in the Rhaetian sandstone, so that operating CAES in this porous formation introduces oxygen in the formation and induces geochemical reactions governed mainly by pyrite oxidation. A consistent geochemical reaction system for the Rhaetian sandstone is developed and kinetic batch simulations are used to quantify the changes due to the induced geochemical reactions in both stored air as well as storage formation.

The injection of air into this geological formation leads to pyrite oxidation, changes in stored air composition, air pressure and formation properties. Results show that only a very small change up to 0.29% in the oxygen mole fraction is found within one storage cycle, which does not affect flammability of the stored air. Considering a longer residence time, the oxygen concentration in the stored air may drop below the minimum oxygen concentration for flame propagation and thus cannot be used for burning natural gas as required for a diabatic CAES. The pH of the formation fluid after 20-year cyclic daily operation can drop significantly below one near the gas wells increasing the risk of well corrosion, but with smaller effects at larger distances. However, mineral dissolution and precipitation found in the storage formation results in only minor increases of porosity and permeability with relative changes up to 1.0% and 5.0%, respectively. The uncertainties in mineral reactive surface area and pyrite oxidation kinetic strongly affect the rate of oxygen reduction and fluid acidification. Analysis of these parameters of the reservoir mineral phases from the target location, especially for pyrite, are therefore required for a reliable estimate of possible induced geochemical reactions and impacts.

## 1. Introduction

As a means of reducing greenhouse gas emission and mitigating climate change effects, renewable energy sources are increasingly substituting fossil fuels. Wind farms and solar power stations are the major sources for renewable energy production, which implies strong fluctuations in electric power generation in the short term due to changing weather conditions and in the longer term due to seasonality effects. To compensate for these fluctuations, a large storage demand of electrical energy is required, with estimates up to 50 TWh for Germany (Bräutigam et al., 2017) or 600 GWh for Denmark aiming for 80% renewable energy share (Sorknæs et al., 2013). Grid-scale standby storage systems in the geological subsurface provide promising storage options, due to their large potential storage capacities, high achievable input and output rates and their flexibility to be employed on time scales varying from hourly to seasonally (Kabuth et al., 2017).

Of these options, large-scale compressed air energy storage (CAES) in the subsurface is one of the gas storage options which is able to compensate strong fluctuations on the hourly to daily basis (Budt et al., 2016). CAES represents a “power to power” energy storage option (Sternberg and Bardow, 2015), which converts off-peak electricity to mechanical energy in the form of pressurized air, stores the compressed air in the subsurface geological formations and retrieves the stored air during times of peak electricity demand to produce power using gas turbines. Currently, only two CAES facilities, i.e. in Huntorf, Germany, and in McIntosh, US, are operating, both using subsurface salt caverns to store the compressed air (Kushnir et al., 2012). Because suitable geological salt formations for mining the required caverns are not widely available but porous formations are more frequently occurring, porous formation storage of compressed air becomes a promising

* Corresponding author.
*E-mail address:* bo.wang@ifg.uni-kiel.de (B. Wang).

https://doi.org/10.1016/j.apgeochem.2019.02.003
Received 22 August 2018; Received in revised form 1 February 2019; Accepted 1 February 2019
Available online 04 February 2019
0883-2927/ 

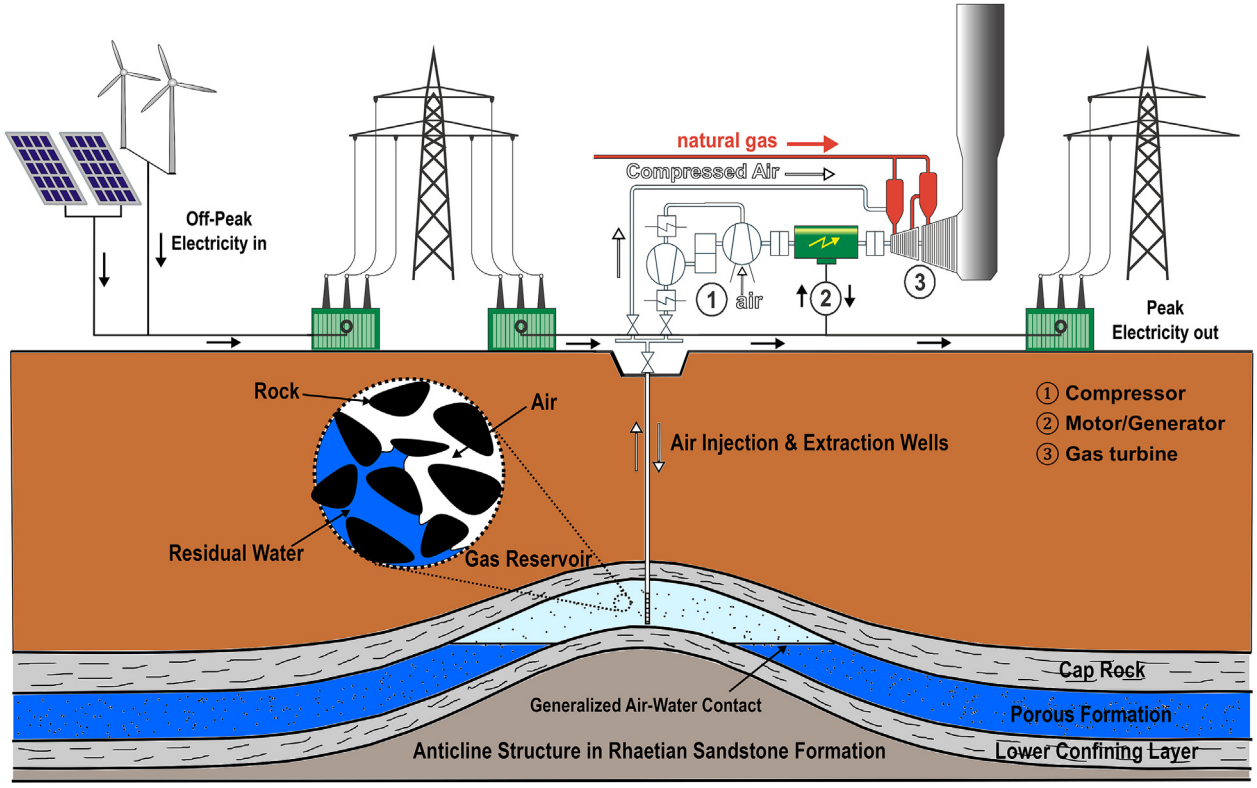


**Fig. 1.** A schematic sketch of a hypothetical conventional CAES facility using a porous formation as the storage reservoir (modified from Wang and Bauer (2017a)).

world-wide option (Succar and Williams, 2008). Moreover, porous formations can provide much larger potential storage capacities (Kabuth et al., 2017). Although currently no CAES in porous formations is operating, the concept has been shown feasible in first studies in the 1980s at a field test site in Pittsfield, Illinois, USA (ANR Storage Company, 1990).

The operation of CAES using porous formations as storage reservoirs is governed by thermal (T), hydraulic (H), mechanical (M) and chemical (C) processes and induces relevant impacts, and a reliable quantification of these is required for designing and dimensioning a storage operation (Bauer et al., 2015, 2013). In terms of the induced hydraulic, mechanic and thermal processes, CAES is comparable to natural gas storage or carbon dioxide capture and storage, which are well known from decades of experience in the oil and gas industry as well as recent research efforts. Anticlinal sites show especially high potential (e.g. Mitiku and Bauer (2013)) for CAES in a porous formation, therefore, the induced pressure is highest as well as lowest at the gas wells and needs to stay within the pressure thresholds for formation damage (Wang and Bauer, 2017a). Due to the expected short operational cycles in CAES, the pressure response during the cyclic operation will be restricted mainly to the gas reservoir (Wang and Bauer, 2017b). The induced temperature change in the storage formation can be limited to only a few Kelvin, as the temperature of injected air from the compressor is cooled down close to the reservoir temperature (Oldenburg and Pan, 2013a). A cyclic operation may introduce cyclic stresses in the formation rock, and Erikson (1983) found a loss of 22% in permeability during the first cycle due to the hysteresis effect for St. Peter sandstone, and much smaller decreases in subsequent cycles as the sandstone shows an elastic behavior.

However, the potentially induced chemical impacts by CAES in a porous formation differ significantly from those of other gas storages, as air containing oxygen is introduced into porous geological formations long-free of oxygen. If redox-sensitive or ferrous-containing minerals are present, such as pyrite ($FeS_2$, iron disulfide), oxidation processes will be induced. These oxidation processes are known from carbon dioxide storage considering oxygen as an impurity (André et al., 2015; Jung et al., 2013; Pearce et al., 2016b, 2016a; Wei et al., 2015), but not studied for the case of CAES applications. Operating CAES in a pyrite containing formations induces pyrite oxidation, and thus the oxygen in the stored air will be partly or completely consumed (ANR Storage Company, 1990). Without a refill of the storage reservoir, the reduced fraction of oxygen in the stored air may potentially cause a failure of a diabatic CAES facility, because the air extracted from the storage may not contain enough oxygen for the gas combustion process required to heat the expanding gas. Studies on acid mine drainage indicate that pyrite oxidation with on-going supply of oxygen, e.g. near gas wells for CAES operation, can lower the pH to very acidic conditions (INAP, 2012; Nordstrom et al., 2015), which thus increases the risk of wellbore corrosion at the gas storage wells. Meanwhile, mineral precipitation induced by geochemical reactions may clog the pore space, thus reducing porosity and permeability of the storage formation, which would again lower the well deliverability and power output (Pei et al., 2015).

Due to these induced geochemical reactions and potential impacts, a reliable quantification of induced geochemical reactions is a prerequisite for assessing the feasibility of porous media CAES. This study therefore focusses on investigating and quantifying potential induced geochemical impacts of a porous formation CAES operation. Potential porous media storage formations are present in the North German Basin (Hese, 2012, 2011), which stretches over parts of Germany, Poland, Denmark, the Netherlands and Great Britain. In this work, the Rhaetian sandstone formation is investigated as a potential storage formation for CAES, as it is well characterized and has been shown suitable in previous research for use in hydrogen storage (Pfeiffer et al., 2017, 2016a; Pfeiffer and Bauer, 2015) or $CO_2$ storage (Mitiku et al., 2013). As the mineral composition of the Rhaetian sandstone shows the presence of pyrite (Dethlefsen et al., 2014; Mitiku et al., 2013), the induced pyrite oxidation and other geochemical reactions are investigated under a consistent geochemical reaction system for the Rhaetian sandstone. The induced impacts on the stored air as well as the storage formation are also quantified using scenario analysis and process based kinetic batch

modelling of such a geochemical system.

## 2. Scenario definition

A synthetic diabatic CAES scenario is used here, assuming the same gas turbine as in the Huntorf power plant. With a minimum inlet pressure of 4.3 MPa, this gas turbine can produce 321 MW of electric power at an air mass flow rate of 417 kg/s and a natural gas mass flow rate of 11 kg/s (E.ON SE, 2016; Hoffeins, 1994; Hoffeins and Mohmeyer, 1986; Kushnir et al., 2012). The natural gas is required to heat the expanded air, which cools considerably in the turbine due to the Joule-Thompson effect. Instead of the two salt caverns used as air storage in the Huntorf power plant, a geometrically representative anticline in the Rhaetian formation in Northern German Basin is assumed to provide a porous storage formation for the compressed air.

A schematic sketch of this synthetic CAES facility is shown in Fig. 1. Before the cyclic operation, an initial fill with air is required to create the gas reservoir in the anticline, as the formation pore space is initially saturated with saline water. This initial fill can be operated with shut-in periods in between to minimize the buoyancy effect and obtain a well-mixed gas phase in the storage reservoir to provide the cushion gas required to support the high injection and extraction rates of such a CAES storage (The HYDROdynamics Group LCC, 2011, 2005). During cyclic operations, when surplus power from renewable resources is available, the motor drives the compressor to compress air, which is then stored in the porous formation. During peak demand, the compressed air is retrieved through the wells from the porous formation. Along with natural gas it is burned in the gas turbine to drive the generator and produce electricity. In this work, the synthetic CAES facility is assumed to operate by a daily cycle for 20 years with a 6-h injection in the early morning and a 6-h extraction in the late afternoon.

The storage reservoir is located in the main sandstone of the Rhaetian formation, which belongs to the Upper Keuper Subgroup (Exter Formation), i.e. the youngest part of the Triassic (Doornenbal and Stevenson, 2010). The Rhaetian storage formation is in this study represented as a highly permeable sandstone with a permeability of $4.93 \times 10^{-13}\,m^2$ and a porosity of 0.35 (see Table 1) according to on-site data provided in Hese (2012, 2011) and the statistical study by Dethlefsen et al. (2014). The top of the storage reservoir is assumed to be located at a depth of 700 m, with a formation thickness of 20 m. The minerals in the Rhaetian sandstone considered here consist of carbonates, silicates, clay mineral K-mica, anhydrite and pyrite (see Table 2), as reported by Mitiku et al. (2013).

In the storage reservoir, the geochemical reactions occur in a multiphase-multicomponent system consisting of a gas phase, i.e. stored air, a liquid phase, i.e. residual formation water, and the solid phase, i.e. the rock and its mineral composition (see Fig. 1). Due to the presence of pyrite in the sandstone, pyrite oxidation is the primary induced geochemical reaction resulting from oxygen dissolution into the formation water. Because the formation water has a high salinity with sodium chloride concentrations of more than some tens of $kg/m^3$, the activity of iron-oxidizing bacteria is strongly reduced (Shiers et al., 2005) and pyrite oxidation here is considered as an abiotic reaction. Without catalyzing iron-oxidizing bacteria, pyrite oxidation is very slow because the oxidation rate of ferrous iron by oxygen to ferric iron is limited at low pH conditions (Singer and Stumm, 1970). At high pH conditions, the solubility of the ferric iron is generally low. Thus, dissolved oxygen is assumed to be the major oxidant for pyrite.

**Table 1**
Parameters of storage formation (Dethlefsen et al., 2014; Hese, 2012, 2011).

| Parameter | Storage Formation |
|---|---|
| Permeability | $4.93 \times 10^{-13}\,m^2$ |
| Porosity | 0.35 |
| Residual Gas Saturation | 0.10 |
| Residual Water Saturation | 0.20 |
| Brooks & Corey Coefficient | 2.5, 0.01 MPa |
| Geothermal Gradient | 25 K/km |
| Water Density | $1050\,kg/m^3$ |
| Rock Density | $2650\,kg/m^3$ |
| Water Compressibility | $0.45\,MPa^{-1}$ |
| Rock Compressibility | $0.45\,MPa^{-1}$ |

**Table 2**
Mineral composition of Rhaetian sandstone formation (Mitiku et al., 2013).

| Minerals | Chemical formula | Concentration [$mol/m^3_{rock}$] | Mass [%] |
|---|---|---|---|
| Albite | $NaAlSi_3O_8$ | $2.03 \times 10^2$ | 1.7 |
| Anhydrite | $CaSO_4$ | $5.37 \times 10^2$ | 2.4 |
| Calcite | $CaCO_3$ | $1.03 \times 10^2$ | 0.3 |
| Dolomite | $CaMg(CO_3)_2$ | $2.05 \times 10^2$ | 1.2 |
| K-feldspar | $KAlSi_3O_8$ | $3.47 \times 10^2$ | 3.1 |
| K-mica | $KAl_3Si_3O_{10}(OH)_2$ | $1.53 \times 10^2$ | 2.0 |
| Pyrite | $FeS_2$ | $1.47 \times 10^3$ | 5.7 |
| Quartz | $SiO_2$ | $4.27 \times 10^4$ | 83.5 |

The designed operation of this hypothetical CAES facility in a porous media formation has been proven to be feasible by Wang and Bauer (2017a, 2017b) in terms of the required pressure at the gas turbine inlet and the corresponding air mass flow rate. They found, that twelve wells are required to sustain the specified target rate of the CAES plant. In this work, the induced impacts on the stored air, the formation fluid and the mineral composition due to geochemical reactions will be addressed and investigated for their impacts by simulating the following “end-member” scenarios:

- For stored air injected and extracted within one storage cycle, geochemical changes are short term and assessed using a residence time of 12 h.
- For stored air from the initial fill and air at the reservoir fringe, longer time scales with a residence time of up to 20 years are applied to assess geochemical changes.
- The potential change in the formation fluid and mineral composition within the gas reservoir is always long term for 20 years, however, near gas wells, it is expected to be driven by a constant supply of oxygen injecting as part of the stored air in each storage cycle.

## 3. Modelling approach

### 3.1. Software

The coupled multiphase-multicomponent ECLIPSE-OpenGeoSys-PHREEQC simulator (see Pfeiffer et al. (2016b)) is used to quantify the induced geochemical reactions and the potential changes in composition of the stored air, the formation fluid and the solid mineral phase. The individual simulations codes used in the coupled simulator are briefly described in the following:

- ECLIPSE is a robust and widely-used reservoir simulators in the oil and gas industry for exploration and production predictions (Schlumberger, 2016). It has been successfully applied to numerical investigation of gas storage options, such as $CO_2$ storage (Benisch and Bauer, 2013; Graupner et al., 2011), hydrogen storage (Pfeiffer et al., 2017) and CAES (Wang and Bauer, 2017a). In this study, ECLIPSE E300 in compositional mode is used to simulate the multiphase-multicomponent air-water system in the storage reservoir by quantifying multicomponent gas flow as well as the phase equilibrium between gas and the formation water.
- OpenGeoSys (www.opengeosys.org) is an open-source, multi-platform finite element based scientific modelling software which can simulate individual and coupled thermal-hydro-mechanical-chemical (THMC) processes in porous and fractured media (Kolditz

et al., 2012; Kolditz and Bauer, 2004). OpenGeoSys has been coupled to chemical reaction software packages, such as ChemApp (Li et al., 2014) and PHREEQC (He et al., 2015), and successfully applied to quantify induced geochemical reactions by $CO_2$ storage (Beyer et al., 2012; Mitiku et al., 2013) or by nuclear waste disposal (Ballarini et al., 2017; Xie et al., 2006). Here, OpenGeoSys is used for coupling ECLIPSE and PHREEQC as well as adapting flow and transport parameters, such as porosity and permeability, due to changes in the mineral composition.

- PHREEQC (version 3) is a computer program for geochemical calculations on speciation, batch-reaction and one-dimensional reactive transport (Parkhurst and Appelo, 2013). It has been applied for quantifying pyrite oxidation reactions in groundwater system (Andersen et al., 2001) and also investigating induced geochemical reactions in storage reservoirs due to $CO_2$ injection (Dethlefsen et al., 2012; Jung et al., 2013). It allows for a range of thermodynamic databases to be used, especially based on the Pitzer approach for highly mineralized fluids. PHREEQC is used in this study to quantify equilibrium and kinetic chemical reactions between the formation water and mineral phase, including mineral dissolution and precipitation.

The coupled ECLIPSE-OpenGeoSys-PHREEQC simulator uses a sequential coupling scheme within each time step. The general time-stepping routine can be briefly summarized as follows:

- Quantify movement of each mobile component in the gas and the water phase using E300. General equations for multiphase flow and mass transport of a component are given as (e.g. Bear and Bachmat (1990); see also Schlumberger (2016)):

$$\frac{\partial(\rho_i \phi S_i)}{\partial t} - \nabla\left(\rho_i \frac{K_{ri}}{\mu_i} K_{in}(\nabla P_i - g\rho_i)\right) = q_i \rho_i \tag{1}$$

where $\rho_i$ [kg/m$^3$] is the density of the phase $i$, $\phi$ [-] the porosity, $S_i$ [-] the saturation, $K_{ri}$ [-] the relative permeability, $\mu_i$ [Pa·s] the viscosity of the phase, $K_{in}$ [m$^2$] the intrinsic permeability, $P_i$ [Pa] the phase pressure, $g$ [m/s$^2$] the gravity constant and $q_i$ [m$^3$/s] the source and sink terms. The component balance is

$$\frac{\partial(\phi S_i C_i^j)}{\partial t} + \nabla(\phi S_i(v_i C_i^j - D_i^j \nabla C_i^j)) - \phi S_i Q_i^j = 0 \tag{2}$$

where $C_i^j$ [mol/m$^3$] the concentration of the component $j$ in phase $i$, $v_i$ [m/s] the phase velocity obtained from Eq. (1), $D_i^j$ [m$^2$/s] the phase and component specific diffusion-dispersion coefficient and $Q_i^j$ the sources/sink term of the component $j$ in phase $i$.

- At each node in OpenGeoSys:
- Assemble molar concentrations of dissolved gas components in the formation water from the current system state as determined by E300. The corresponding equation is:

$$C_{j,w} = \frac{MLSC_j * 1000}{S_w} - S_g \frac{YFW_j * \rho_{g,\,res}}{MW_j * S_w} \tag{3}$$

where $C_{j,w}$ [mol/m$^3_w$] is the concentration of component $j$ in the formation water, $MLSC_j$ [kmol/m$^3_{pv}$] the molar concentration of component $j$ in the total pore volume of one element, $S_w$ [-] and $S_g$[-] the saturation of the water and gas phase, respectively, $MW_j$ [kg/mol] the molar weight of the component, $\rho_{g,\,res}$ [kg/$m_g^3$] the density of gas phase at reservoir conditions and $YFW_j$ [$kg_j$/$kg_g$] the mass fraction of the component in the gas phase.

- Assemble molar concentrations of dissolved components in the formation water and mineral components in the solid phase from PHREEQC results from the last time step.
- Simulate kinetically controlled chemical reactions using PHREEQC (see Eq. (12)).
- Update molar concentrations in the formation water and the solid phase
- Quantify feedbacks for E300 on flow and transport related parameters, i.e. porosity and permeability, using a Kozeny-Carman porosity-permeability model (Bear, 2013) as:

$$\phi_{t+\Delta t} = \phi_t + (1 - \phi_t) \sum_{n}^{nt} [MV^n(m_t^n - m_{t+\Delta t}^n)] \tag{4}$$

$$K_{in\_t} = K_{in\_t0}\left(\frac{1 - \phi_{t0}}{1 - \phi_t}\right)^2 \left(\frac{\phi_t}{\phi_{t0}}\right)^3 \tag{5}$$

where $\phi_t$ [-] is the porosity at a given time $t$, $nt$ the total number of minerals, $MV^n$ [$m^3_{rock}$/mol] the molar volume of mineral $n$, $m^n$ [mol] the moles of mineral $n$, $K_{in\_t0}$ [m$^2$] the initial intrinsic permeability and $K_{in\_t}$ [m$^2$] the intrinsic permeability at a given time $t$.

- Proceed to next time step.

### 3.2. Reservoir batch model

A reservoir batch model with a constant volume is set up to quantify potential changes of the stored air composition for different residence times, as well as changes in the storage formation at the reservoir fringe. This batch model accounts for changes in stored air pressure and composition, by considering a constant volume of porous formation of 100 m$^3$. To quantify the change in the storage formation near gas wells, a constant air flow rate in the model accounting for the on-going supply of air from each storage cycle is included.

The depth of the reservoir batch model is at 710 m representing the average depth of the storage formation. The corresponding parameters are listed in Table 1 (Dethlefsen et al., 2014; Hese, 2012, 2011), and the capillary pressure-saturation function of the reservoir is determined by a Brooks and Corey correlation (Brooks and Corey, 1964). The water density is 1050 kg/m$^3$ representing a salinity of ~70 kg/m$^3$ at a depth of 710 m (Delfs et al., 2016). The reservoir batch model is initially equilibrated with the prior filled air at a hydrostatic pressure of 7.09 MPa. Reservoir temperature is 306.15 K, assuming a surface temperature 288.15 K and a geothermal gradient of 25 K/km.

The air forming the cushion gas has a composition of 78.15% $N_2$, 20.90% $O_2$, 0.91% Ar and 0.04% $CO_2$. Air properties are calculated in E300 using a generalized form of the Peng-Robinson equations of state (Schlumberger, 2016) and the compositional gas parameters listed in Table 3. The solubility of air components in the formation fluid are calculated by the methods described in the work from Mitiku et al. (2013) and Li et al. (2018) accounting for the salinity of the formation fluid as well as reservoir temperature and pressure. Evaporation of

**Table 3**
Parameters of air components (Kaye and Laby, 2016; Lemmon et al., 2000).

| Parameter | $N_2$ | $O_2$ | Ar | $CO_2$ |
|---|---|---|---|---|
| Critical Temperature | 126.192 K | 154.581 K | 150.687 K | 304.18 K |
| Critical Pressure | 3.39 MPa | 5.04 MPa | 4.86 MPa | 7.38 MPa |
| Critical Molar Volume | $8.95 \times 10^{-5}$ m$^3$/mol | $7.34 \times 10^{-5}$ m$^3$/mol | $7.46 \times 10^{-5}$ m$^3$/mol | $9.19 \times 10^{-5}$ m$^3$/mol |
| Acentric Factor | 0.037 | 0.022 | −0.002 | 0.224 |

residual water is not considered here, so that the residual water saturation remains constant during the simulation. The air in this batch model thus has a total volume of 27.36 $m^3$ and a weight of 2247 kg at a density of 82.11 $kg/m^3$. The air components are 592.43 $mol/m^3$ of $O_2$, 1.01 $mol/m^3$ of $CO_2$, 2215.64 $mol/m^3$ of $N_2$ and 26.01 $mol/m^3$ of Ar. For the case of on-going supply of air, an air volume flow rate of 0.016 $m^3/s$ at reservoir conditions is applied to represent the air exchange during one storage cycle.

### 3.3. Geochemical batch model

#### 3.3.1. Thermodynamic database

The thermodynamic database for PHREEQC geochemical calculations is based on the 6th released database from THEREDA (Altmaier et al., 2011), which uses the PITZER interaction model (Pitzer, 1973) to account for activities in a high salinity condition and also includes aqueous species related to carbonate and silicate minerals. The corresponding parameters of PITZER interaction model for iron mineral related species, such as $Fe^{2+}$, $Fe^{3+}$ and $S^{2-}$, are added based on the study by Cohen et al. (1987) and Moog and Hagemann (2004). The influence of pressure and temperature changes on solution species and mineral phases is not considered in the database. These effects are expected to be small due to limited temperature and pressure changes during a cyclic CAES storage operation.

#### 3.3.2. Equilibrated geochemical system

The mineral assemblage (see Table 2) for the Rhaetian sandstone is taken from a statistical study by Dethlefsen et al. (2014), while the reference fluid composition (see Table 4) represents measured values for the Rhaetian sandstone from an average depth of 1500 m (Mitiku et al., 2013). An equilibrated geochemical system is derived by the stepwise addition of minerals and adjustment of the solution species. The equilibrated fluid composition (Table 4) has a pH of 6.96, indicating a pH-neutral environment. Concentrations of $Na^+$ and $Cl^-$ are adjusted explicitly to represent the lower solubility of 70 $kg/m^3$ at 710 m depth and are thus lower than in the reference fluid. The equilibrated concentration of $SO_4^{2-}$ is one order of magnitude higher, because anhydrite is considered as a primary mineral instead of gypsum, and its solubility is larger at the formation temperature of 306.15 K (Klimchouk, 1996). The lower concentration of $Fe^{2+}$ is due to the lower solubility of pyrite at the lower pressure and temperature conditions at smaller depth. The differences of other equilibrated concentrations to the measured data are within one order of magnitude, which is attributable to uncertainties in sampling and is within the range of the spatial variation (Dethlefsen et al., 2014). The equilibrated concentrations of solution species can thus be considered as a representative fluid composition in the Rhaetian sandstone.

**Table 4**
Fluid chemistry of Rhaetian sandstone formation: reference data and equilibrated results.

| Species | Reference Concentration (Mitiku et al., 2013) [$mol/m^3_{liquid}$] | Equilibrated Concentration [$mol/m^3_{liquid}$] |
|---|---|---|
| $Al^{3+}$ | Not measured | $1.67 \times 10^{-5}$ |
| $CO_3^{2-}$ | Not measured | $6.04 \times 10^{-1}$ |
| $Ca^{2+}$ | $6.83 \times 10^{1}$ | $1.38 \times 10^{2}$ |
| $Cl^-$ | $2.69 \times 10^{3}$ | $1.56 \times 10^{3}$ [a] |
| $Fe^{2+}$ | $3.00 \times 10^{-1}$ | $1.37 \times 10^{-4}$ |
| $K^+$ | 6.80 | 4.72 |
| $Mg^{2+}$ | $3.21 \times 10^{1}$ | $7.65 \times 10^{1}$ |
| $Na^+$ | $2.51 \times 10^{3}$ | $1.20 \times 10^{3}$ [a] |
| $SO_4^{2-}$ | 9.40 | $3.63 \times 10^{1}$ |
| $Si^{4+}$ | Not measured | $1.07 \times 10^{-1}$ |
| pH [-] | Not measured | 6.96 |

[a] Concentration is adjusted explicitly considering the salinity of formation fluid at the reservoir condition.

#### 3.3.3. Primary and secondary minerals

Minerals (see Table 2) used for equilibrating the geochemical system of the Rhaetian sandstone formation are considered as primary minerals. The secondary iron-related minerals resulting from pyrite oxidation are selected based on studies on acid mine drainage. The chemical reaction for induced pyrite oxidation is shown in Eq. (6) (Chandra and Gerson, 2010; Lowson, 1982; Taylor et al., 2009). At a pH larger than 3.5, insoluble ferric hydroxide ($Fe(OH)_3$) is precipitated due to hydrolysis (see Eq. (7)) (Nordstrom, 1982). Insoluble ferric hydroxide is in an amorphous state and will continuously transform to other mineral forms, such as goethite (see Eq. (8)), ferryhydrite, schwertmannite, hematite and jarosite (see Eq. (9)). Among these minerals, goethite is the most stable mineral phase over the pH range 2–6 compared to schwertmannite and ferryhydrite (Bigham et al., 1996). Hematite is formed only under a dehydration process of ferric hydroxide at temperatures close to 373.15 K (Cornell and Schwertmann, 2003). This temperature is much higher than the temperature in the storage formation. In a strong acid solution with a low pH (e.g. pH $<$ 2) and rich in sulfate and ferric ions, potassium jarosite ($KFe_3(OH)_6(SO_4)_2$)may precipitate (Cornell and Schwertmann, 2003; Zolotov and Shock, 2005). For the secondary iron-related minerals, therefore, we consider goethite as representing the minerals containing oxidized ferric iron at all pH conditions, and jarosite for the minerals buffering the solution with a high concentration of $H^+$ and $SO_4^{2-}$ at a pH of lower than 2.0.

$$FeS_2 + {}^{15}\!/_{4}O_{2(aq)} + {}^{1}\!/_{2}H_2O \rightarrow Fe^{3+} + 2SO_4^{2-} + H^+ \quad (6)$$

$$Fe^{3+} + 3H_2O \rightarrow Fe(OH)_{3(a)} + 3H^+ \quad (7)$$

$$Fe(OH)_{3(a)} \rightarrow FeOOH_{(goethite)} + H_2O \quad (8)$$

$$K^+ + 3Fe(OH)_{3(a)} + 2SO_4^{2-} + 3H^+ \rightarrow KFe_3(OH)_6(SO_4)_{2(jarosite)} + 3H_2O \quad (9)$$

Pyrite oxidation produces acid, i.e. the hydrogen ion $H^+$ (see Eq. (6)). The $H^+$ can react with the carbonates calcite and dolomite in the Rhaetian sandstone formation and induce carbonate dissolution (Appelo and Postma, 2005) (see Eq. (10) and Eq. (11)). Concentrations of $Ca^{2+}$ and $SO_4^{2-}$ in solution will increase and precipitation of anhydrite is expected. The clay mineral kaolinite ($Al_2Si_2O_5(OH)_4$) is chosen as the secondary mineral for mineral precipitation when the solution has a high concentration of $Al^{3+}$, following the study by Mitiku et al. (2013).

$$CaCO_{3(calcite)} + 2H^+ \rightarrow Ca^{2+} + H_2O + CO_2 \quad (10)$$

$$CaMg(CO_3)_{2(dolomite)} + 4H^+ \rightarrow Ca^{2+} + Mg^{2+} + 2H_2O + 2CO_2 \quad (11)$$

According to Palandri and Kharaka (2004), the dissolution rate constant of silicates and clay minerals is often very slow and roughly six orders of magnitude lower than the rate for carbonates, anhydrite and pyrite. For quantifying the potential change in stored air with the constant volume batch model, preliminary model runs show that including silicates and clay minerals has no significant impact on the simulated results. Therefore, the dissolution of silicates and clay minerals is neglected. However, as preliminary model results near gas wells show that the pH of the formation fluid may drop below 1.0, precipitation of jarosite and dissolution of the silicate mineral K-feldspar and the clay mineral K-mica for balancing potassium concentration may occur. Therefore, these reactions and minerals have to be considered when quantifying the changes near a gas well.

#### 3.3.4. Reaction kinetics

The general rate law for mineral dissolution and precipitation can be written as (Appelo and Postma, 2005):

$$dm/dt = -A_{react} \times k \times g(c) \times \left(1 - IAP/K\right) \quad (12)$$

where $dm/dt$ shows the overall reaction rate in [mol/s] and $m$ [mol] is the moles of mineral at a given time $t$ [s]. $k$ [mol/m$^2$/s] is the specific rate constant, $A_{react}$ [m$^2$] the mineral reactive surface area referring to 1 kg water assumed in PHREEQC, $g(c)$ [-] a function accounting for the effects of the solution composition (Lasaga, 1998), such as i.e. pH, *IAP* [-] the ion activity product, and $K$ [-] the solubility product. The ratio $IAP/K$ indicates the saturation state of a mineral, and $\left(1 - IAP/K\right)$ determines whether minerals are dissolving or precipitating by changing the sign of Eq. (12).

The reactive surface area $A_{react}$ can be estimated from geometrical considerations as (Klein et al., 2013):

$$A_{react} = \alpha \times A_{geom} \times m \times M_s \quad (13)$$

where, $\alpha$ [-] is a factor accounting for the selective sites of mineral surface area involving in reactions, $M_s$ [kg/mol] the molar weight of minerals and $A_{geom}$ [m$^2$/kg] the mineral geometric surface area per kg of mineral. The geometric surface is calculated assuming mineral particles are spheres (Cantucci et al., 2009; Klein et al., 2013):

$$A_{geom} = r \times 6/(\rho_s \times d_s) \quad (14)$$

where, $\rho_s$ [kg/m$^3$] is the mineral density, $d_s$ [m] the average grain diameter and r [-] a factor accounting for the roughness on mineral surfaces. If assuming a smooth surface, r equals one.

The average grain diameter for non-clay minerals is set to $2 \times 10^{-5}$ m and for clay minerals to $2 \times 10^{-6}$ m (see Klein et al. (2013); Cantucci et al. (2009); Gaus et al. (2005)). A factor of 10 is used here to quantify the true geometric surface area accounting for the roughness on the mineral surface (White and Peterson, 1990), as also shown in the studies by Zerai et al. (2006), Zhang et al. (2009) and Xu et al. (2010). The $\alpha$factor in Eq. (13) is applied to account for a reduced reactivity due to smaller reactive surface areas in natural environments (Beckingham et al., 2016; Bourg et al., 2015). In this study, a factor of $10^{-3}$ is applied for primary minerals following studies by Klein et al. (2013), Gaus et al. (2005), Zhang et al. (2009) and Xu et al. (2010). For secondary minerals, a factor of $10^{-1}$ is used assuming a very large contact surface area with the fluids. Besides, a very small amount of about $1 \times 10^{-8}$ mol is initially given in the model for secondary minerals as a 'seed' concentration to allow for precipitation. This results in an initial surface area of $1 \times 10^{-6}$ ($m^2/m^3_{rock}$), in accordance with work by Mitiku et al. (2013) and Zhang et al. (2009). The calculated reactive surface areas for primary and secondary minerals are listed in Table 5.

Except pyrite and jarosite, the specific rate constant $k$ together with the function $g(c)$, i.e. the term $k{\cdot}g(c)$, for all primary and secondary minerals are formulated according to Palandri and Kharaka (2004). The relevant data for all minerals are listed in Table 5. The well-established rate law from Williamson and Rimstidt (1994) written as Eq. (15) is applied here for quantifying the rate of pyrite oxidation. It is valid for aqueous pyrite oxidation by dissolved $O_2$ referring to Eq. (6).

$$k \times g(c) = 10^{-8.19} \times m_{DO}^{0.5}/m_{H^+}^{0.11} \quad (15)$$

where $m_{DO}$ [mol] is the mole of dissolved oxygen and $m_{H^+}$ [mol] the mole of hydrogen ions.

For jarosite, a specific rate constant of $1.00 \times 10^{-10}$ mol/m$^2$/s as given by Brookfield et al. (2006) is applied in Eq. (12) for the term $k \times g(c)$. Additionally, a condition of pH < 2.0 is added in the formulation of the rate law as an indicator allowing the precipitation of jarosite for a solution rich of $H^+$ and $SO_4^{2-}$.

## 4. Results

### 4.1. Short- and long-term change in the stored air pressure and composition

The kinetic batch model using the concept of constant volume was applied to investigate the short- and long-term changes of stored air pressure and air composition due to induced geochemical reactions. As one storage cycle consists of 6 h of air injection and 6 h of air extraction, air has a residence time of 12 h in the gas reservoir. Two different reservoir pressures were used, with 7.10 MPa representing the average pressure during one storage cycle and 10.65 MPa representing the highest occurring pressure and thus the case of highest $O_2$ solubility.

Results are reported in Table 6 and show that at a pressure of 7.10 MPa, 4.91 mol of $O_2$ in the injected air is used to oxidize pyrite and the produced $H^+$ reacts with carbonates resulting in a production of 4.60 mol of $CO_2$. The difference in oxygen is due to precipitation of the mineral goethite. This corresponds to a relative reduction of 0.03% for oxygen and a relative increase of 16.48% for $CO_2$, respectively. At the higher pressure of 10.65 MPa, the absolute changes are larger due to the higher amount of dissolved $O_2$, however the relative changes are even smaller with 0.02% and 12.82%, respectively.

For a diabatic CAES, the oxygen loss in the stored air can affect the flammability of the gas mixture of extracted air and the added natural gas. According to Zabetakis (1964), at a pressure of 4.3 MPa, which is the inlet pressure of the Huntorf gas turbine, the minimum oxygen concentration (MOC) required for flame propagation in a gas mixture of natural gas, nitrogen and oxygen is approximately 9.5%, both in volume or moles. Therefore the change in $O_2$ during one cycle will not

**Table 5**
Kinetic rate parameters for primary and secondary minerals.

| Parameter | $A_{react}$ [m$^2$/g] | Kinetic rate parameters (Brookfield et al., 2006; Palandri and Kharaka, 2004) | | | | | | | |
|---|---|---|---|---|---|---|---|---|---|
| | | Neutral mechanism | | Acid mechanism | | | Base mechanism | | |
| | | $k_{25}$ [mol/m$^2$/s] | $E_a$ [kJ/mol] | $k_{25}$ [mol/m$^2$/s] | $E_a$ [kJ/mol] | n($H^+$) | $k_{25}$ [mol/m$^2$/s] | $E_a$ [kJ/mol] | n($H^+$) |
| Primary Minerals | | | | | | | | | |
| Anhydrite | $1.01 \times 10^{-3}$ | $6.46 \times 10^{-4}$ | 14.3 | | | | | | |
| Calcite | $1.11 \times 10^{-3}$ | $1.55 \times 10^{-6}$ | 23.5 | $5.01 \times 10^{-1}$ | 14.4 | 1.0 | $3.31 \times 10^{-4}$ | 35.4 | 1.0[a] |
| Dolomite | $1.06 \times 10^{-3}$ | $2.95 \times 10^{-8}$ | 52.2 | $6.46 \times 10^{-4}$ | 36.1 | 0.5 | $1.13 \times 10^{-3}$ | | |
| Quartz | $1.13 \times 10^{-3}$ | $1.02 \times 10^{-14}$ | 87.7 | | | | | | |
| Albite | $1.15 \times 10^{-3}$ | $2.75 \times 10^{-13}$ | 69.8 | $6.92 \times 10^{-11}$ | 65.0 | 0.46 | $2.51 \times 10^{-16}$ | 71.0 | −0.57 |
| K-Feldspar | $1.17 \times 10^{-3}$ | $3.89 \times 10^{-13}$ | 38.0 | $8.71 \times 10^{-11}$ | 51.7 | 0.5 | $6.31 \times 10^{-22}$ | 94.1 | −0.82 |
| K-Mica | $1.02 \times 10^{-2}$ | $1.00 \times 10^{-13}$ | 22.0 | | | | | | |
| Pyrite | $5.99 \times 10^{-4}$ | Rate law from Williamson and Rimstidt (1994) (Eq. (15)) | | | | | | | |
| Secondary minerals | | | | | | | | | |
| Goethite | $7.89 \times 10^{-2}$ | $1.15 \times 10^{-8}$ | 86.5 | | | | | | |
| Jarosite | $9.80 \times 10^{-2}$ | $1.00 \times 10^{-10}$ | | | | | | | |
| Kaolinite | 1.15 | $6.92 \times 10^{-14}$ | 22.2 | $4.90 \times 10^{-12}$ | 65.9 | 0.78 | $8.91 \times 10^{-18}$ | 17.9 | −0.47 |

[a] Reaction order n with respect to partial pressure of CO2.

**Table 6**
Change in components $O_2$ and $CO_2$ within one storage cycle of 12 h at reservoir pressures of 7.10 MPa and 10.65 MPa.

| Air Pressure | Time | $O_2$ | $CO_2$ | $\Delta O_2$ | | $\Delta CO_2$ | |
|---|---|---|---|---|---|---|---|
| [MPa] | [hour] | [mol] | [mol] | [mol] | [%] | [mol] | [%] |
| **7.10** | **0** | 16209.64 | 27.88 | −4.91 | −0.03% | 4.60 | 16.48% |
| | **12** | 16204.73 | 32.48 | | | | |
| **10.65** | **0** | 24333.60 | 43.25 | −5.75 | −0.02% | 5.55 | 12.82% |
| | **12** | 24327.85 | 48.80 | | | | |

affect the flammability of the stored air mixed with the natural gas.

To investigate long-term changes in the stored air, the kinetic batch model was run for a simulation time of 20 years assuming a reservoir pressure of 7.10 MPa. The resulting changes in air pressure and air composition are shown in Fig. 2. The oxygen mole fraction drops below MOC after about 4.6 years (see Fig. 2b) and the stored air cannot be used for burning natural gas. For even longer residence times, the air pressure drops further to 6.32 MPa after about 14.5 years and remains constant afterwards, as all oxygen has been depleted by the reactions. Pressure decreases, because the gas density of $CO_2$ is higher than of $O_2$. Furthermore, although the kinetic reaction rates of pyrite oxidation are similar to those of carbonate dissolution, the induced chemical reactions result in a decrease of 1 mol of $O_2$ but a corresponding increase of less than 1 mol of $CO_2$ due to the precipitation of goethite. $N_2$ and Ar are not participating in the chemical reactions, so their absolute mole numbers remain constant. However, due to the net decrease of moles in $O_2$ and $CO_2$, the total moles of gas components in the stored air decreases, resulting in an increase in $N_2$ and Ar mole fractions.

### 4.2. Change in the formation fluid and minerals within the gas reservoir

Air is brought to the edge of the gas reservoir during the initial fill, but is not replaced by the cyclic storage operation due to the long distance from the well. This causes a limited supply of oxygen, as oxygen is not replenished, and thus a different reactive behavior compared to the places near gas wells. The kinetic batch model with the concept of the constant volume is thus suitable to investigate the change in the formation fluid and minerals at the reservoir edge for a simulation time of 20 years. The pH of the formation fluid (see Fig. 3a) shows a fast decrease from the initial value of 6.96 to 5.48 within the first two years. Pyrite oxidation producing acid lowers the pH even with buffering by carbonate dissolution, because the produced $CO_2$ stays in the gas phase with an elevated partial pressure and thus has a higher solubility. After the $O_2$ in the stored air is completely consumed at about 14.5 years (see Fig. 2b), pH drops to 5.12 and remains constant afterwards. This demonstrates that pyrite oxidation can acidize the formation fluid, but pH will not drop further due to the limited supply of oxygen.

At a pH of 5.12 jarosite does not precipitate and thus jarosite, silicates and clay minerals are not considered in this case. Fig. 3a shows changes in solution species concentration of those species relevant to carbonates, anhydrite and iron minerals. The concentration of $Ca^{2+}$ increases for about 7 years and decreases again afterwards. The increase results from the dissolution of calcite and dolomite (see Fig. 3b) due to the additional $H^+$ from pyrite oxidation. The enrichment of $Ca^{2+}$ in the solution results in the precipitation of anhydrite which reduces the concentration of $SO_4^{2-}$ at the same time. After the complete dissolution of calcite at about 7 years (see Fig. 3b), the precipitation of anhydrite causes a decrease of the concentration of $Ca^{2+}$. The anhydrite precipitation rate decreases due to a slower supply of $Ca^{2+}$ from dolomite dissolution, which leads to an increase in $SO_4^{2-}$ concentration. At the same time, the additional $H^+$ from pyrite oxidation can only react with dolomite, which shows as a faster increase of $Mg^{2+}$ in the solution. The total concentration of Fe, i.e. the sum of $Fe^{2+}$ and $Fe^{3+}$, is not observable in Fig. 3a because the small amount of $Fe^{2+}$ in the initial solution is quickly oxidized by the dissolved $O_2$ and the $Fe^{3+}$ from pyrite oxidation is precipitated as goethite (see Fig. 3b). The weight percentage of pyrite used in this reaction up to MOC is about 0.15%.

Near the gas wells fresh air containing oxygen is supplied in each storage cycle. This situation is simulated using the kinetic batch model with constant air flow. Due to this constant supply, the dissolved $O_2$ concentration remains constant (Fig. 4b). After about 12.5 years pH decreases from 6 to 1.5 (see Fig. 4a) when dolomite in the mineral phase has been completely dissolved (see Fig. 4c) and $H^+$ from pyrite oxidation cannot be buffered any more by carbonate minerals. The resulting acidic solution shows an increase in the concentration of Fe as $Fe^{3+}$, because goethite precipitation stops but pyrite oxidation still continues, as well as a further slow reduction in pH. A low pH in the solution also leads to the slow dissolution of silicate and clay minerals, which shows as an increase of $Si^{4+}$ concentration and later $K^+$ concentration. The solution species of $Ca^{2+}$, $Mg^{2+}$ and $SO_4^{2-}$ show the same behavior as in the case of no oxygen resupply (see Fig. 3a), but the overall change in concentration is much larger. During air extraction, some of the residual low pH formation fluid near the extraction well may be produced together with the air. The acidified formation fluid is thus in contact with the well inner tubing and increases the risk of corrosion in the gas well. This effect needs to be considered when

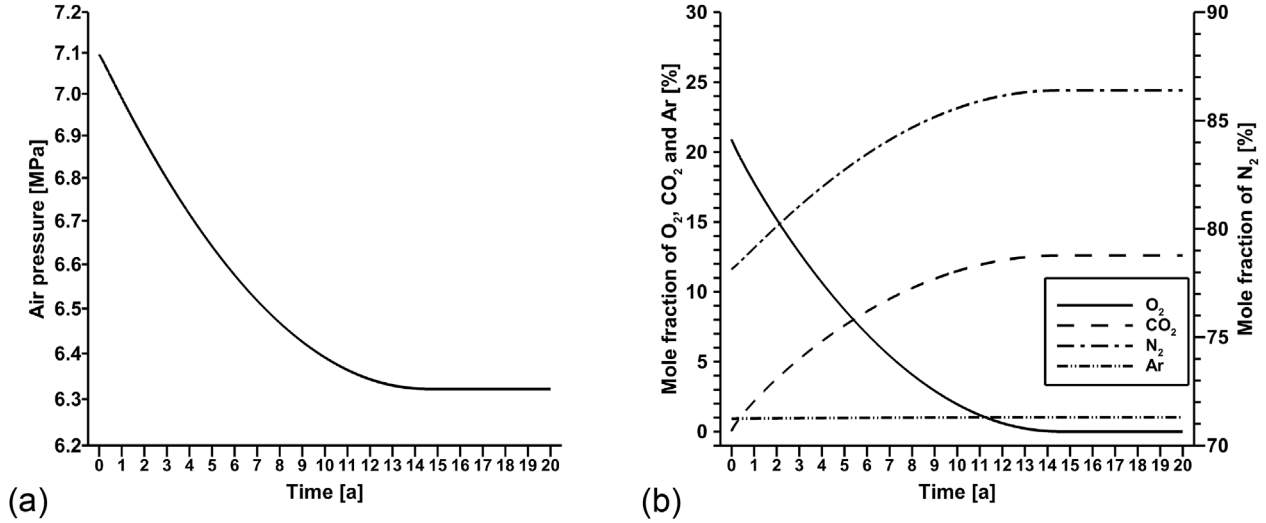


**Fig. 2.** Change in the stored air without oxygen replenishment. (a) air pressure (b) air components.

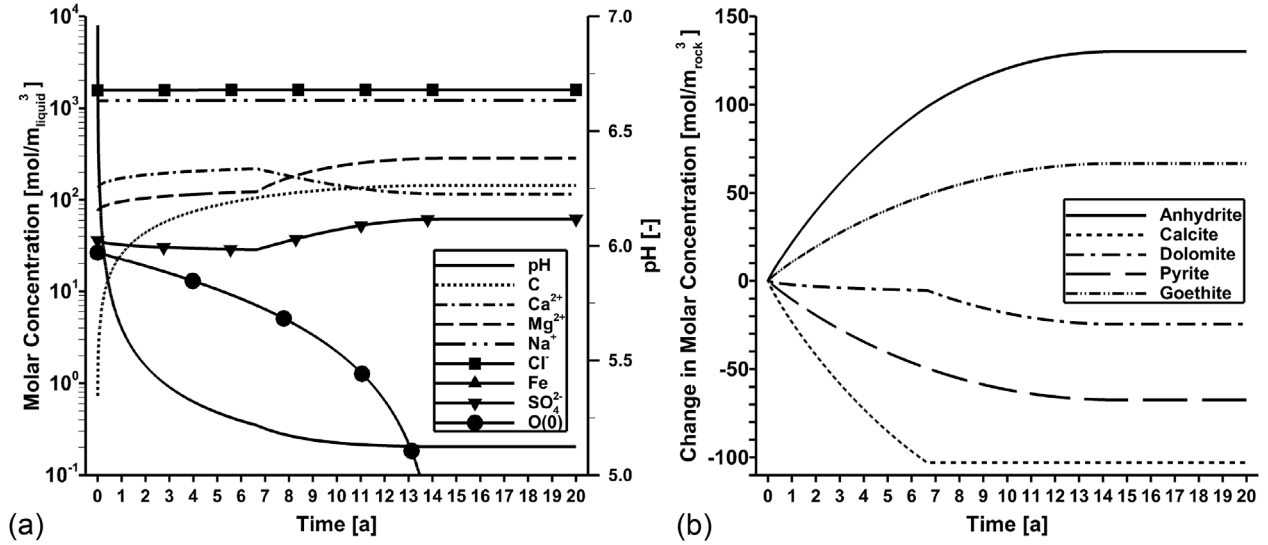


**Fig. 3.** Geochemical composition of formation water and storage formation without oxygen replenishment. (a) pH and solution species of formation fluid (b) formation minerals.

selecting appropriate materials for the gas well materials.

Due to the produced acid, pyrite oxidation leads to a complete dissolution of calcite after approximately 5.3 years and for dolomite after approximately 12.5 years (see Fig. 4c). A 60% increase in the molar concentration of anhydite can be found after 20 years, due to the enrichment of $Ca^{2+}$ and $SO_4^{2-}$ concentration in the pore fluid. The relative change in silicate minerals, such as quartz, is less than 1% (see Fig. 4d) due to the small change of porosity. Approximately 6% of the mineral K-mica has dissolved after 20 years, resulting in an increase of the K+ concentration in solution. After 20 years, about 12% of pyrite has reacted with the dissolved $O_2$. The iron-containing minerals goethite, jarosite and the clay mineral kaolinite are therefore precipitating (see Fig. 4e). The precipitated goethite starts to dissolve after the pH of the formation fluid reaches around 2.0, which also leads to the precipitation of kaolinite and jarosite. Overall mineral dissolution and precipitation in the storage formation result in only a small increase of porosity and thus permeability, with relative changes of about 0.3% and 1.2% respectively (see Fig. 4f). These small changes in porosity and permeability induce only a minor impact on the deliverable air flow rate, i.e. the maximum air pumping rate of the storage reservoir. A slight decrease is found after 12.5 years, when all carbonates have been dissolved and kaolinite as well as jarosite start to precipitate.

## 5. Sensitivity analysis

### 5.1. Influence of mineral reactive surface area

Parametrization of geochemical reactions in geochemical models involves a range of uncertainties, as e.g. the amount of pyrite reactive surface area may spatially vary strongly. During the Rhaetian time, the depositional system in the Northern German Basin changed spatially from a non-marine system in the east through a paralic system in the middle to a marine setting in the west (Doornenbal and Stevenson, 2010). These sedimentary conditions typically lead to a strong variation in grain sizes and grain morphologies of the pyrite deposited, implying an uncertainty of the reactive mineral surface area. The possible range of pyrite reactive surface area as reported by Bourg et al. (2015) is between $4 \times 10^{-2}\,m^2/g$ and $1 \times 10^{-4}\,m^2/g$. Thus, larger surface areas than the value of $5.99 \times 10^{-4}\,m^2/g$ used in this study are possible. Here, we assume a roughness factor of 10 and a $\alpha$ factor of $10^{-2}$ to represent a larger reactive surface area of $5.99 \times 10^{-3}\,m^2/g$. For comparison, a roughness factor of 1 and a factor $\alpha$ of $10^{-3}$ is applied to represent a smooth geometric surface area of mineral grains with a smaller reactive surface area of $5.99 \times 10^{-5}\,m^2/g$.

#### 5.1.1. Impact on short- and long-term changes of stored air pressure and composition

Accounting for different mineral reactive surface areas, the change in $O_2$ and $CO_2$ of the injected air within one storage cycle of 12 h is shown in Table 7. Within one storage cycle, the $O_2$ in the injected air can decrease by 0.003% at the smaller reactive surface area and up to 0.29% at the larger reactive surface area, at a pressure of 7.10 MPa $CO_2$ increases accordingly by 1.98% and 144.78%, respectively. Therefore, even using a larger reactive surface area of $5.99 \times 10^{-3}\,m^2/g$, the loss of $O_2$ in the injected air within one storage cycle will not affect the flammability of the stored air mixed with the natural gas either.

Considering a longer residence time of 20 years, using a larger mineral reactive surface area of $5.99 \times 10^{-3}\,m^2/g$ leads to a pressure drop of 0.78 MPa within about 1.8 years (Fig. 5a) as well as the total depletion of oxygen in the stored air (Fig. 5b). MOC in the stored air is reached after already half a year, which is shorter than the time required for the initial fill of the gas reservoir. This faster decrease also increases the risk of failure during operation of this diabatic CAES, as the stored air cannot be used for burning natural gas. However, lower reaction rates are also possible using a smaller reactive surface area of $5.99 \times 10^{-5}\,m^2/g$, which leads to a pressure drop of only 0.22 MPa even after 20 years (Fig. 5a) and an oxygen mole fraction of 15% (Fig. 5b). The depletion rate of $O_2$ in the stored air and the air pressure are thus very sensitive to the mineral reactive surface area, and for a reliable estimate of these changes, the analysis of this parameter of minerals from a target geological formation is thus required.

#### 5.1.2. Impact on the porous storage formation

At the edge of the reservoir, where no oxygen is replenished during the cyclic operation, using a larger mineral reactive surface area of $5.99 \times 10^{-3}\,m^2/g$ leads to a faster pH decrease to 5.12 within about 1.8 years. The pH remains constant afterwards as all oxygen has been consumed then (Fig. 6a). After 20 years, using a smaller mineral reactive surface area of $5.99 \times 10^{-5}\,m^2/g$, the pH has decreased to 5.47. The pH will further decrease until all oxygen has been consumed and will also reach 5.12 as in the other cases. If oxygen is not replenished, a different reactive surface area only influences the rate of pH decrease but not the final magnitude.

However, near gas wells with a constant supply of oxygen containing fresh air, using a smaller reactive surface area of

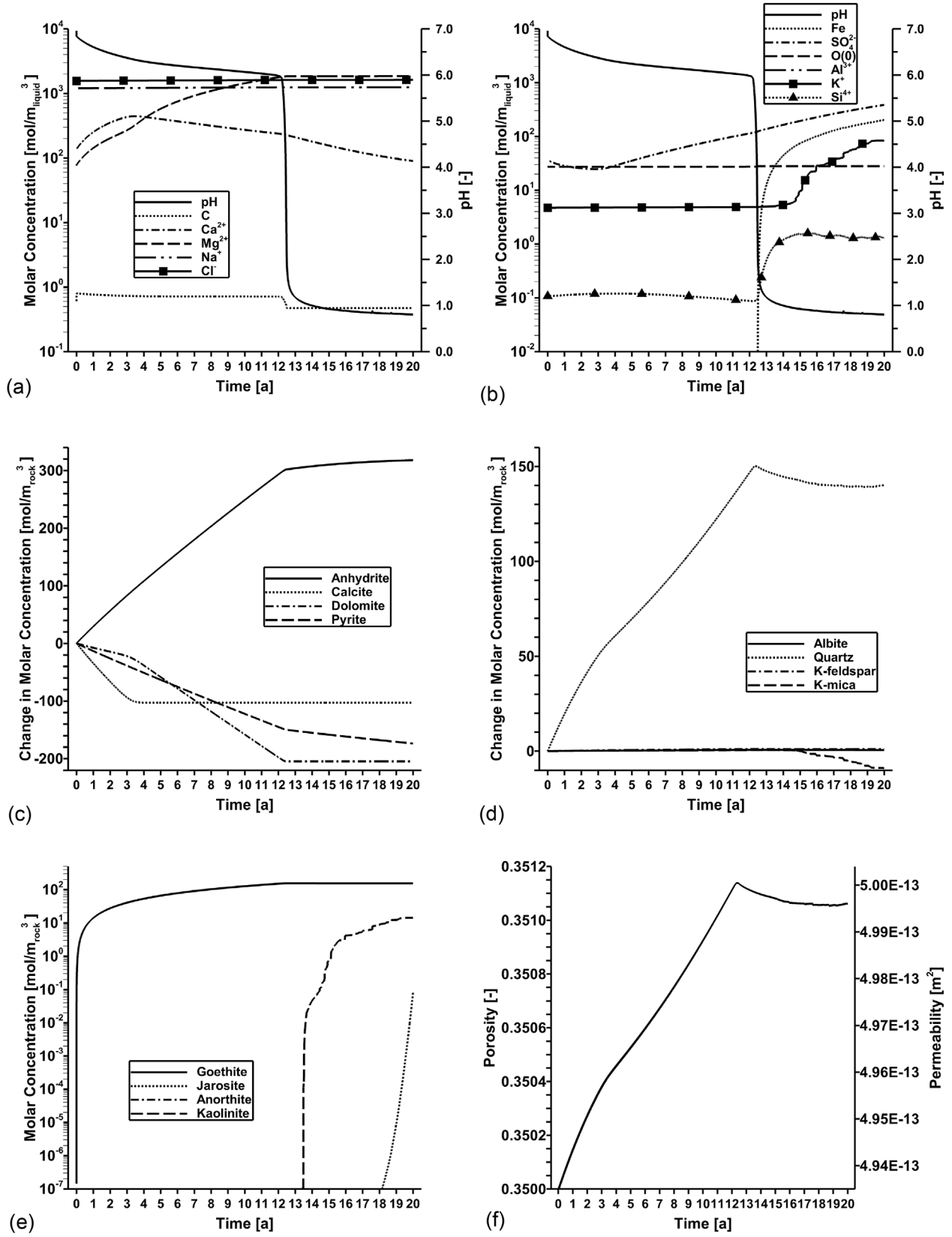


**Fig. 4.** Geochemical composition of formation water and storage formation with oxygen replenishment. (a, b) pH and solution species of formation fluid (c, d) primary mineral compositions (e) secondary mineral compositions (f) porosity and permeability.

**Table 7**
Change in components of $O_2$ and $CO_2$ within one storage cycle of 12 h at reservoir pressure of 7.10 MPa and 10.65 MPa accounting for different mineral reactive surface areas.

| Air Pressure | Time | $A_{react}$ | $O_2$ | $CO_2$ | $\Delta O_2$ | | $\Delta CO_2$ | |
|---|---|---|---|---|---|---|---|---|
| [MPa] | [hour] | [$m^2$/g] | [mol] | [mol] | [mol] | [%] | [mol] | [%] |
| **7.10** | **0** | | 16209.64 | 27.88 | | | | |
| | **12** | **$5.99 \times 10^{-5}$** | 16209.12 | 28.43 | −0.52 | −0.003% | 0.55 | 1.98% |
| | | **$5.99 \times 10^{-4}$** | 16204.73 | 32.48 | −4.91 | −0.03% | 4.60 | 16.48% |
| | | **$5.99 \times 10^{-3}$** | 16163.60 | 68.25 | −46.04 | −0.29% | 40.37 | 144.78% |
| **10.65** | **0** | | 24333.60 | 43.25 | | | | |
| | **12** | **$5.99 \times 10^{-5}$** | 24333.01 | 43.82 | −0.59 | −0.002% | 0.57 | 1.32% |
| | | **$5.99 \times 10^{-4}$** | 24327.85 | 48.80 | −5.75 | −0.02% | 5.55 | 12.82% |
| | | **$5.99 \times 10^{-3}$** | 24279.13 | 92.59 | −54.47 | −0.22% | 49.34 | 114.06% |

$5.99 \times 10^{-5}$ $m^2$/g only causes a pH decrease to 6.58 after 20 years (Fig. 6b), which is even higher than the case without oxygen replenishment. This is because the $CO_2$ produced is extracted from the gas reservoir during each operation cycle. Therefore $CO_2$ partial pressure and solubility do not increase, as in the case without air replenishment. Using the larger reactive surface area, pH drops to 0.8 after about 2 years, and thus the risks of corrosion in the gas wells is increased substantially already at the beginning of the cyclic operation. The overall mineral dissolution and precipitation reactions induced in the storage formation result in relative increases of 1% and 5% of porosity and permeability after 20 years, as shown in Fig. 6c. This represents minor changes and thus will only slightly affect well deliverability.

### 5.2. Influence of pyrite mineral surface passivation

As pyrite oxidation is mainly a mineral surface controlled reaction (Chandra and Gerson, 2010), the hydrolytic precipitation of ferric-ion-containing hydroxide may form a passivation layer on the pyrite mineral surface. Results from lab experiments on pyrite oxidation (Berta et al., 2016; Huminicki and Rimstidt, 2009; Pérez-López et al., 2009) showed that carbonates present in the mineral or fluid phase reduce the reaction rate of pyrite oxidation due to the formation of a passivation layer. In the Rhaetian sandstone formation considered here, the mineral composition shows the presence of carbonate minerals together with pyrite, and these carbonates may help to form the passivation layer on the surface of pyrite.

Accounting for surface passivation in the model, the loss of $O_2$ of the stored air may be strongly reduced. To quantify this passivation effect, we applied a rate law for pyrite oxidation accounting for the surface passivation from Berta et al. (2016) (see Eq. (16)). This rate law also accounts for the influence by the partial pressure of $O_2$ in the gas phase.

$$k{\cdot}g(c) = (f_{rest} + f_{pass}{\cdot}pass){\cdot}k_{WR} \tag{16}$$

where, $f_{rest}$ [-] is the fraction of un-passivated pyrite, $f_{pass}$ [-] the fraction of passivated pyrite, $k_{WR}$ [mol/$m^2$/s] the rate law from Williamson and Rimstidt as shown in Eq. (15). The factor *pass* is given by Berta et al. (2016) as:

$$pass = \left(1 - \frac{m_0 - m}{m_0}{\cdot}f_1{\cdot}e^{f_2{\cdot}P_{O_2}}\right)^{f_3} \quad and\ 1 \geq pass \geq 0 \tag{17}$$

where, $m_0$ [mol] is the initial moles of pyrite, $m$ [mol] the moles of pyrite at a given time, $P_{O_2}$ [MPa] the partial pressure of $O_2$, and $f_1$[-], $f_2$[-] and $f_3$[-] fitted parameters as 100, -0.015 and 0.75, respectively.

#### 5.2.1. Impact on short- and long-term changes of stored air pressure and composition

Considering the surface passivation of pyrite, at a pressure of 7.10 MPa only 0.006% of $O_2$ in the injected air has reacted (Table 8). This value is five times smaller than in the case without surface passivation. The produced acid reacting with carbonates leads to a relative increase of 3.47% $CO_2$ in the injected air. At the higher pressure of 10.65 MPa, the relative changes are 0.004% and 2.47%, respectively. Because of surface passivation, the changes of $O_2$ and $CO_2$ in the injected air within one storage cycle are much smaller, which will not affect the flammability of the stored air mixed with the natural gas.

Considering a longer residence time of 20 years, pressure of the

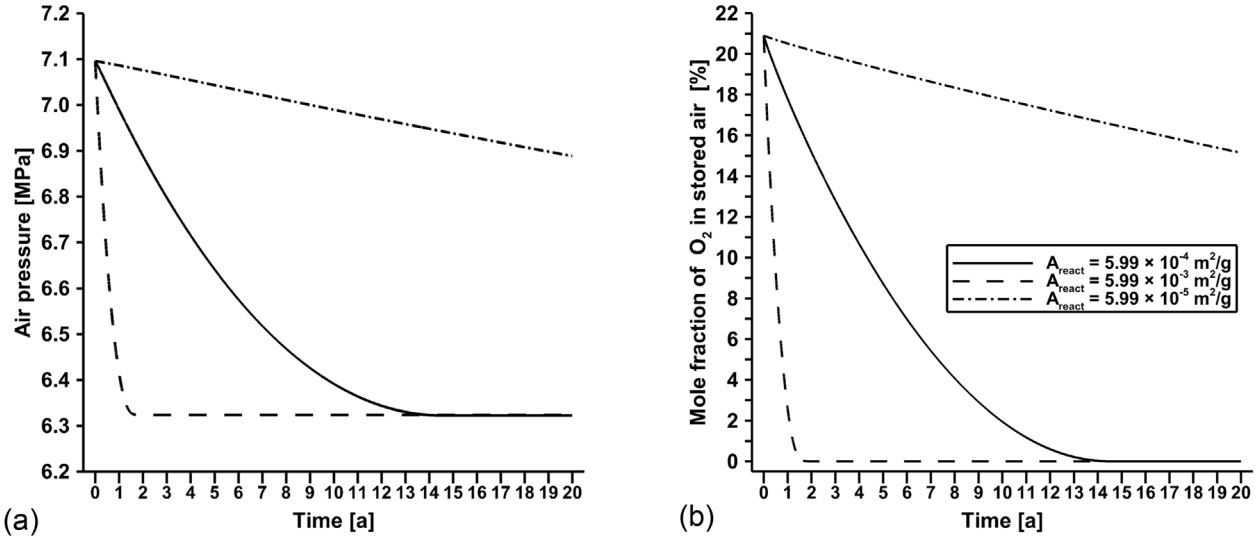


**Fig. 5.** Influence of mineral reactive surface area on the change in the stored air without oxygen replenishment. (a) air pressure (b) oxygen mole fraction.

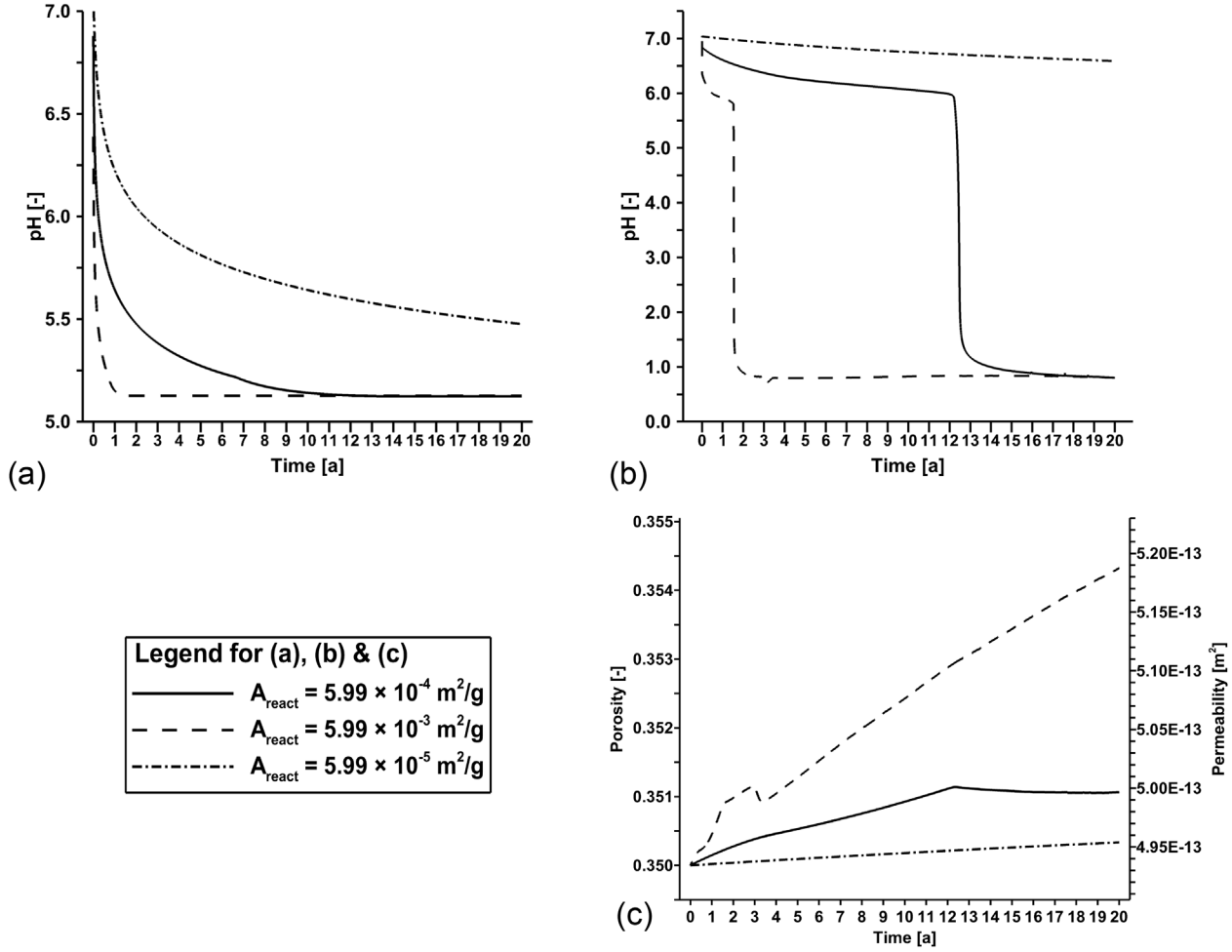


**Fig. 6.** Influence of mineral reactive surface area on the change in the storage formation. (a) pH without oxygen replenishment (b) pH with oxygen replenishment (c) porosity and permeability with oxygen replenishment.

stored air decreases to 6.94 MPa (see Fig. 7a) accounting for the surface passivation on pyrite, and the corresponding mole fraction of $O_2$ in the stored air is 16.4% (see Fig. 7b). The same amount of change in oxygen can be observed at about 1.5 years without the surface passivation, which shows that the formed passivation layer strongly reduces the oxygen depletion rate. Thus, in the case of surface passivation occurring, the mole fraction of $O_2$ in the stored air is decreasing only slightly even for longer residence time, and values are always above MOC. Because the oxygen depletion rate is strongly determined by the kinetics of pyrite oxidation, experimental tests for a target formation are required to reliably quantify these impacts.

*5.2.2. Impact on the porous storage formation*

At the edge of the reservoir without oxygen replenishment, accounting for the surface passivation of pyrite leads to a pH decrease to 5.54 after 20 years (Fig. 8a) which is close to the fluid pH of 5.12 considering no surface passivation. Because oxygen is not replenished at the reservoir fringe, surface passivation does not significantly change the pH of the formation fluid there.

Near gas wells with a constant supply of fresh oxygen containing air, however, accounting for surface passivation stabilizes pH at a neutral value of 6.56 even after 20 years (Fig. 8b). This strongly reduces the risks of corrosion in the gas wells for the operation of CAES. Correspondingly, after 20 years, overall mineral dissolution and precipitation in the storage formation causes relative changes of only 0.08% and 0.40% in porosity and permeability (see Fig. 8c). This effect is thus very small and does not change well deliverability.

**Table 8**
Change in components of $O_2$ and $CO_2$ within one storage cycle of 12 h at reservoir pressure of 7.10 MPa and 10.65 MPa accounting for surface passivation.

| Air Pressure | Time | Pyrite oxidation kinetic | $O_2$ | $CO_2$ | $\Delta O_2$ | | $\Delta CO_2$ | |
|---|---|---|---|---|---|---|---|---|
| [MPa] | [hour] | | [mol] | [mol] | [mol] | [%] | [mol] | [%] |
| **7.10** | **0** | | 16209.64 | 27.88 | | | | |
| | **12** | **no passivation** | 16204.73 | 32.48 | −4.91 | −0.03% | 4.60 | 16.48% |
| | | **with passivation** | 16208.67 | 28.85 | −0.97 | −0.006% | 0.97 | 3.47% |
| **10.65** | **0** | | 24333.60 | 43.25 | | | | |
| | **12** | **no passivation** | 24327.85 | 48.80 | −5.75 | −0.02% | 5.55 | 12.82% |
| | | **with passivation** | 24332.53 | 44.32 | −1.07 | −0.004% | 1.07 | 2.47% |

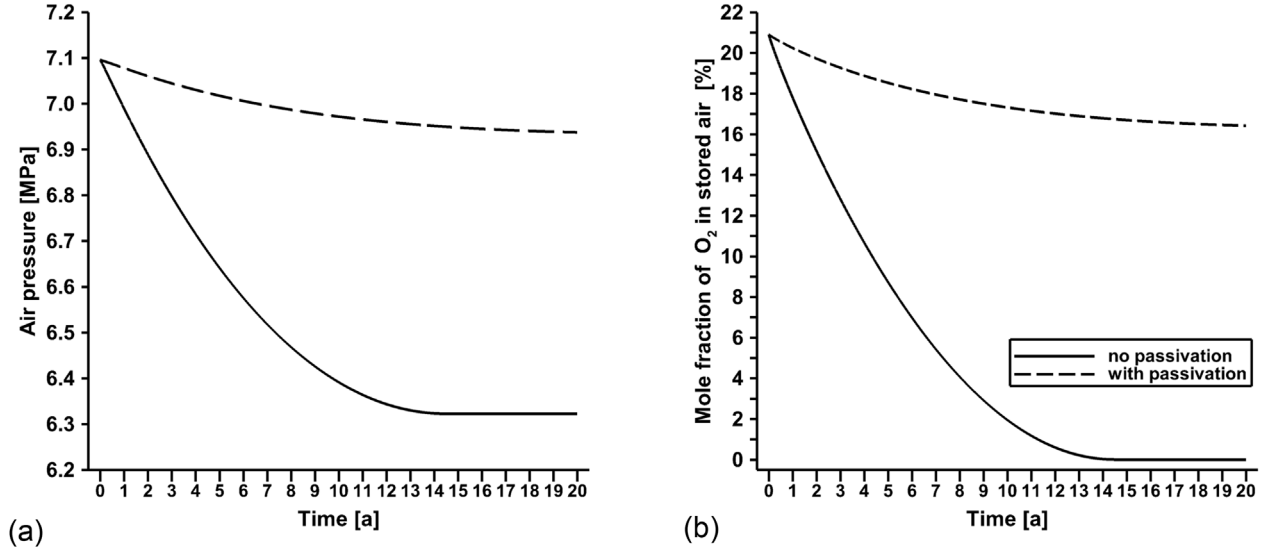


**Fig. 7.** Influence of mineral surface passivation on the change in the stored air without oxygen replenishment. (a) air pressure (b) oxygen mole fraction.

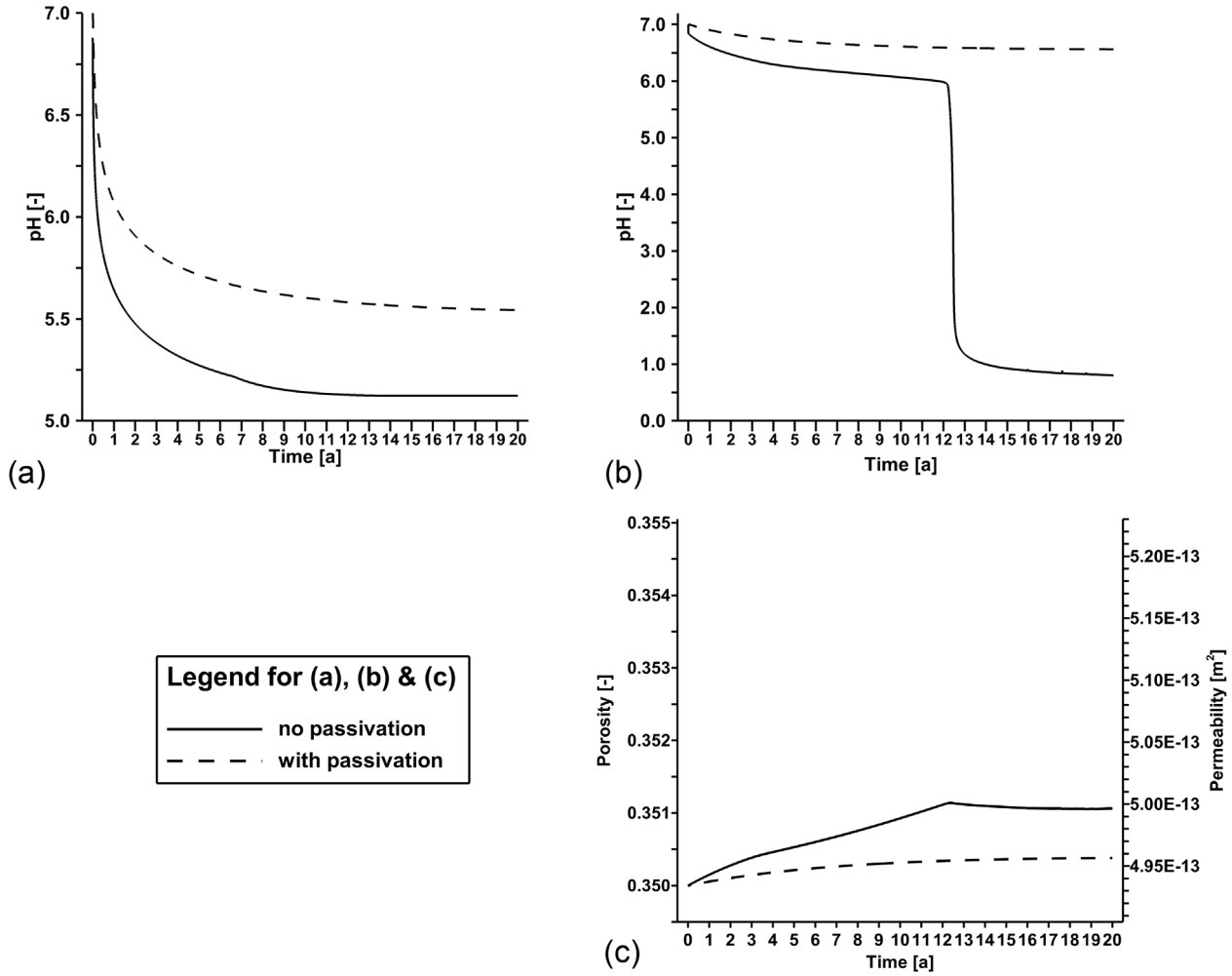


**Fig. 8.** Influence of mineral surface passivation on the change in the storage formation. (a) pH without oxygen replenishment (b) pH with oxygen replenishment (c) porosity and permeability with oxygen replenishment.

## 6. Discussion

### 6.1. Gas phase mixing in the storage reservoir

The short-term changes in stored air composition during one storage cycle assessed using the kinetic batch model show a very small decrease in oxygen content due to the induced geochemical reactions. This shows that on this short time scale no geochemical impacts on storage operation will occur. The long-term changes in stored air composition however indicate that the mole fraction of oxygen in stored air may be reduced to below MOC and even to zero at large time scales. In this case, an operation failure of the diabatic CAES facility will occur. This can be mitigated by a refill of fresh, oxygen rich air. These two models represent the "end members" of the spectrum of residence times that will occur in a gas storage reservoir. In a real porous gas storage formation, however, mixing between injected fresh air and air stored for longer times will occur. These mixing effects are not explicitly considered here by a full reservoir model, as they will depend strongly on the geometric and hydrodynamic characteristics of the storage formation. Thus, general findings on this mixing cannot be derived, but mixing effects are discussed in the following.

The mole fraction of $O_2$ in the extracted air will be between the two bounding cases considered here, providing a lower power output in the early stages of storage use than indicated by the short-term model. This effect is also found by Oldenburg and Pan (2013b), who considered porous formation CAES using $CO_2$ as cushion gas and found that in the case of 20 m air-$CO_2$ interface noticeable amounts of $CO_2$ were produced along with the extracted air during the first production cycle. With on-going cyclic operation, however, the mole fraction of $O_2$ in the extracted air will increase as oxygen mixed into the gas reservoir in prior cycles is recovered along with the short-term stored air. Some of the oxygen will diffuse to the reservoir fringe, due to the concentration gradient in the storage air, and supply somewhat more oxygen there than considered in the long-term simulations without gas flow. This may result in a stronger decrease of pH there than given by the current model. The extent of oxygen mixing and diffusion in the gas phase will thus also depend on the storage cycles used.

### 6.2. Mineral assemblage of the Rhaetian sandstone

In this study, one possible mineral assemblage is chosen to represent the mineral composition in the Rhaetian sandstone. Using other minerals, such as gypsum instead of anhydrite, or, gibbsite instead of kaolinite, would slightly change the simulation results, but would not change the basic findings of this study, such as oxygen reduction due to induced geochemical reactions. However, the amount of redox-sensitive minerals available in the mineral assemblage, here represented by pyrite, may affect the amount of oxygen reduction in the gas phase. The available core samples from the Rhaetian sandstone show amounts of pyrite in the mineral composition varying between zero and up to 6% (Dethlefsen et al., 2014). Therefore, the amount of pyrite is likely lower than the 5.7% assumed here, which would reduce the geochemical impacts accordingly. If the pyrite content is less than 0.15%, oxygen concentrations will always remain above MOC, which means that air can be stored for long. However, if organic carbon or other ferrous-containing minerals are present, the induced geochemical reactions may still result in a reduction of oxygen concentration below MOC because they can also react with oxygen.

### 6.3. Impact of residual water saturation

Gas dissolution in the residual formation water in the porous storage formation is considered here as an equilibrium process, because a small residual water saturation of 0.2 is assumed. If larger residual water saturation occur, the travel time for the dissolved oxygen to the mineral surfaces, where the reactions occur, as well as the respective travel time of carbon dioxide towards the gas phase, are increasing strongly. Accounting for this diffusion controlled transport process for the dissolved gas components would thus further limit the reaction rates and the oxygen consumption. Therefore, at larger residual water saturations in the storage formation the depletion rate of $O_2$ in the stored air and the power reduction rate will be slower than shown here. The model used here is thus conservative with respect to this effect.

The cyclic injection of dry air may lead to evaporation of the residual water and thus a reduction of water saturation or a complete dry out near the wells. The induced geochemical reactions in the storage formation would thus be further reduced or even stopped when the formation is fully dehydrated, as the reactions can only occur if water is present. This would increase the relative permeability for gas flow and thus storage performance, as higher rates can be obtained. At the same time, the precipitation of all dissolved minerals in this dry out zone may reduce permeability and porosity, which would counter this effect.

## 7. Conclusions

A synthetic diabatic compressed air energy storage (CAES) based on the existing Huntorf facility and employing the Rhaetian sandstone formation in the North German Basin as porous storage reservoir is investigated for induced geochemical reactions. The chosen mineral assemblage shows the presence of pyrite in the Rhaetian sandstone, so that CAES in this porous formation will induce geochemical reactions mainly governed by pyrite oxidation. A geochemical reaction system for the Rhaetian sandstone is developed and kinetic batch simulations are used to quantify the changes in stored air as well as the storage formation due to the induced geochemical reactions. The major conclusions that can be drawn are:

(1) The ECLIPSE-OGS-PHREEQC coupling scheme can be applied to quantify the induced geochemical reactions for CAES in porous formations with a consistent geochemical system. It can be scaled up to a reactive reservoir scale model.
(2) Within one storage cycle, i.e. 12 h residence time in the storage formation, oxygen loss in stored air is found to be very small. This minor oxygen loss does not affect the flammability of the stored air mixed with natural gas and thus will not influence the cyclic operation of CAES.
(3) For longer residence times, the oxygen mole fraction can drop below the minimum oxygen concentration (MOC) required for flame propagation. Then this stored air cannot be used for burning natural gas directly, and the risk of operating failure without an intermediary refill occurs. Thus an adiabatic CAES may be a preferable option for porous formation storage, as heat gained during air compression is stored and can be used to heat the extracted air during expansion, instead of burning natural gas to this end.
(4) The pH of the formation fluid may drop significantly near wells, even to values below 1.0. The acidified fluid increases the risks of well corrosion and should be considered when selecting the casing material of the gas wells.
(5) The induced dissolution and precipitation of minerals results only in a minor increase of porosity and permeability, which will not affect the storage performance in terms of well deliverability.
(6) The uncertainties in mineral assemblage, mineral reactive surface area and pyrite oxidation kinetic strongly affect the rate of oxygen reduction and fluid acidification. Analysis of these parameters of the reservoir mineral phases from the target location, especially for pyrite, are therefore required for a reliable estimate of possible induced geochemical reactions and impacts
(7) The geochemical reaction system investigated here represents the first step to quantify the induced geochemical impacts of CAES using kinetic batch simulations. Mixing between the injected air and the stored air could be quantified using the presented reaction scheme and a reactive reservoir flow and transport model.

## Acknowledgements

We gratefully acknowledge the funding of the ANGUSII joint project by the German Federal Ministry of Economic Affairs and Energy (BMWi) (grant number 03ET6122A), as well as the support of the Project Management Jülich (PTJ). We also thank Dr. Christof Beyer, Dr. Dedong Li, Dr. Wolf Tilmann Pfeiffer and Dr. Markus Ebert for all the great help and the fruitful discussions with them.

## Appendix A. Supplementary data

Supplementary data to this article can be found online at https://doi.org/10.1016/j.apgeochem.2019.02.003.

## References

Altmaier, M., Brendler, V., Bube, C., Marquardt, C., Moog, H.C., Richter, A., Scharge, T., Voigt, W., Wilhelm, S., 2011. THEREDA. Thermodynamic Reference Database.Final Report. GRS-265.

Andersen, M.S., Larsen, F., Postma, D., 2001. Pyrite oxidation in unsaturated aquifer sediments. Reaction stoichiometry and rate of oxidation. Environ. Sci. Technol. 35, 4074–4079. https://doi.org/10.1021/es0105919.

André, L., Azaroual, M., Bernstone, C., Wittek, A., 2015. Modeling the Geochemical Impact of an Injection of CO2 and Associated Reactive Impurities (SO2 and O2) into a Saline Reservoir. Transport Porous Media 108, 185–205. https://doi.org/10.1007/s11242-014-0359-7.

ANR Storage Company, 1990. Compressed-air energy storage: Pittsfield aquifer field test; Test data: engineering analysis and evaluation. Detroit, Michigan.

Appelo, C., Postma, D., 2005. Geochemistry, Groundwater and Pollution, second ed. Taylor & Francis. https://doi.org/10.1201/9781439833544.

Ballarini, E., Graupner, B., Bauer, S., 2017. Thermal–hydraulic–mechanical behavior of bentonite and sand-bentonite materials as seal for a nuclear waste repository: Numerical simulation of column experiments. Appl. Clay Sci. 135, 289–299. https://doi.org/10.1016/j.clay.2016.10.007.

Bauer, S., Beyer, C., Dethlefsen, F., Dietrich, P., Duttmann, R., Ebert, M., Feeser, V., Görke, U., Köber, R., Kolditz, O., Rabbel, W., Schanz, T., Schäfer, D., Würdemann, H., Dahmke, A., 2013. Impacts of the use of the geological subsurface for energy storage: an investigation concept. Environ. Earth Sci. 70, 3935–3943. https://doi.org/10.1007/s12665-013-2883-0.

Bauer, S., Pfeiffer, T., Boockmeyer, A., Dahmke, A., Beyer, C., 2015. Quantifying induced effects of subsurface renewable energy storage. Energy Procedia 76, 633–641. https://doi.org/10.1016/j.egypro.2015.07.885.

Bear, J., 2013. Dynamics of fluids in porous media. Courier Corporation.

Bear, J., Bachmat, Y., 1990. Introduction to modeling of transport phenomena in porous media. Kluwer Academic Publishers, AA Dordrecht, The Netherlands.

Beckingham, L.E., Mitnick, E.H., Steefel, C.I., Zhang, S., Voltolini, M., Swift, A.M., Yang, L., Cole, D.R., Sheets, J.M., Ajo-Franklin, J.B., DePaolo, D.J., Mito, S., Xue, Z., 2016. Evaluation of mineral reactive surface area estimates for prediction of reactivity of a multi-mineral sediment. Geochem. Cosmochim. Acta 188, 310–329. https://doi.org/10.1016/j.gca.2016.05.040.

Benisch, K., Bauer, S., 2013. Short- and long-term regional pressure build-up during CO2 injection and its applicability for site monitoring. Int. J. Greenh. Gas Control 19, 220–233. https://doi.org/10.1016/j.ijggc.2013.09.002.

Berta, M., Dethlefsen, F., Ebert, M., Gundske, K., Dahmke, A., 2016. Surface passivation model explains pyrite oxidation kinetics in column experiments with up to 11 bars p (O2). Environ. Earth Sci. 75, 1175. https://doi.org/10.1007/s12665-016-5985-7.

Beyer, C., Li, D., De Lucia, M., Kühn, M., Bauer, S., 2012. Modelling CO2-induced fluid–rock interactions in the Altensalzwedel gas reservoir. Part II: coupled reactive transport simulation. Environ. Earth Sci. 67, 573–588. https://doi.org/10.1007/s12665-012-1684-1.

Bigham, J.M., Schwertmann, U., Traina, S.J., Winland, R.L., Wolf, M., 1996. Schwertmannite and the chemical modeling of iron in acid sulfate waters. Geochem. Cosmochim. Acta 60, 2111–2121. https://doi.org/10.1016/0016-7037(96)00091-9.

Bourg, I.C., Beckingham, L.E., DePaolo, D.J., 2015. The nanoscale basis of CO2 trapping for geologic storage. Environ. Sci. Technol. Lett. 49, 10265–10284. https://doi.org/10.1021/acs.est.5b03003.

Bräutigam, A., Rothacher, T., Staubitz, H., Trost, R., 2017. The Energy Storage Market in Germany Small-scale Battery Systems.

Brookfield, A.E., Blowes, D.W., Mayer, K.U., 2006. Integration of field measurements and reactive transport modelling to evaluate contaminant transport at a sulfide mine tailings impoundment. J. Contam. Hydrol. 88, 1–22. https://doi.org/10.1016/j.jconhyd.2006.05.007.

Brooks, R., Corey, A., 1964. Hydraulic properties of porous media. Hydrol. Pap. Color. State Univ. 3 37 pp.

Budt, M., Wolf, D., Span, R., Yan, J., 2016. A review on compressed air energy storage: Basic principles, past milestones and recent developments. Appl. Energy 170, 250–268. https://doi.org/10.1016/j.apenergy.2016.02.108.

Cantucci, B., Montegrossi, G., Vaselli, O., Tassi, F., Quattrocchi, F., Perkins, E.H., 2009. Geochemical modeling of CO2 storage in deep reservoirs: The Weyburn Project (Canada) case study. Chem. Geol. 265, 181–197. https://doi.org/10.1016/j.chemgeo.2008.12.029.

Chandra, A.P., Gerson, A.R., 2010. The mechanisms of pyrite oxidation and leaching: A fundamental perspective. Surf. Sci. Rep. 65, 293–315. https://doi.org/10.1016/j.surfrep.2010.08.003.

Cohen, M.D., Flagan, R.C., Seinfeld, J.H., 1987. Studies of concentrated electrolyte solutions using the electrodynamic balance. 1. Water activities for single-electrolyte solutions. J. Phys. Chem. 91, 4563–4574. https://doi.org/10.1021/j100301a029.

Cornell, R.M., Schwertmann, U., 2003. Formation. In: The Iron Oxides. Wiley-VCH Verlag GmbH & Co. KGaA, Weinheim, FRG, pp. 345–364. https://doi.org/10.1002/3527602097.ch13.

Delfs, J.-O., Nordbeck, J., Bauer, S., 2016. Upward brine migration resulting from pressure increases in a layered subsurface system. Environ. Earth Sci. 75, 1441. https://doi.org/10.1007/s12665-016-6245-6.

Dethlefsen, F., Ebert, M., Dahmke, A., 2014. A geological database for parameterization in numerical modeling of subsurface storage in northern Germany. Environ. Earth Sci. 71, 2227–2244. https://doi.org/10.1007/s12665-013-2627-1.

Dethlefsen, F., Haase, C., Ebert, M., Dahmke, A., 2012. Uncertainties of geochemical modeling during CO 2 sequestration applying batch equilibrium calculations. Environ. Earth Sci. 65, 1105–1117. https://doi.org/10.1007/s12665-011-1360-x.

Doornenbal, H., Stevenson, A., 2010. Petroleum geological atlas of the Southern Permian Basin area. EAGE, Houten, the Netherlands.

E.ON SE, 2016. Kraftwerk Huntorf. [WWW Document]. (accessed 2.17.16). http://www.eon.com/de/ueber-uns/struktur/asset-finder/huntorf-power-station.html.

Erikson, R.L., 1983. Thermophysical Behavior of St . Peter Sandstone : Application to Compressed Air Energy Storage in an Aquifer. Richland, Washington.

Gaus, I., Azaroual, M., Czernichowski-Lauriol, I., 2005. Reactive transport modelling of the impact of CO2 injection on the clayey cap rock at Sleipner (North Sea). Chem. Geol. 217, 319–337. https://doi.org/10.1016/j.chemgeo.2004.12.016.

Graupner, B.J., Li, D., Bauer, S., 2011. The coupled simulator ECLIPSE–OpenGeoSys for the simulation of CO2 storage in saline formations. Energy Procedia 4, 3794–3800. https://doi.org/10.1016/j.egypro.2011.02.314.

He, W., Beyer, C., Fleckenstein, J.H., Jang, E., Kolditz, O., Naumov, D., Kalbacher, T., 2015. A parallelization scheme to simulate reactive transport in the subsurface environment with OGS#IPhreeqc 5.5.7-3.1.2. Geosci. Model Dev 8, 3333–3348. https://doi.org/10.5194/gmd-8-3333-2015.

Hese, F., 2012. 3D Modellierungen und Visualisierung von Untergrundstrukturen für die Nutzung des unterirdischen Raumes in Schleswig-Holstein. PhD Thesis. University of Kiel, Germany.

Hese, F., 2011. Geologische 3D-modelle des untergrundes schleswig-holsteins – ein beitrag für potenzialstudien zur nutzung von tiefen salinen aquiferen. Zeitschrift der Dtsch. Gesellschaft für Geowissenschaften 162, 389–404. https://doi.org/10.1127/1860-1804/2011/0162-0389.

Hoffeins, H., 1994. Huntorf Air Storage Gas Turbine Power Plant. Energy Supply - Brown Boveri Mittelungen Publication No.D GK 90 202 E.

Hoffeins, H., Mohmeyer, K.-U., 1986. Operating experience with the Huntorf air-storage gas turbine power station. Brown Boveri Mittelungen Publication No.D GK 1274 86 E.

Huminicki, D.M.C., Rimstidt, J.D., 2009. Iron oxyhydroxide coating of pyrite for acid mine drainage control. Appl. Geochem. 24, 1626–1634. https://doi.org/10.1016/j.apgeochem.2009.04.032.

INAP, 2012. Global Acid Rock Drainage Guide , INAP. The International Network for Acid Prevention.

Jung, H.B., Um, W., Cantrell, K.J., 2013. Effect of oxygen co-injected with carbon dioxide on Gothic shale caprock-CO2-brine interaction during geologic carbon sequestration. Chem. Geol. 354, 1–14. https://doi.org/10.1016/j.chemgeo.2013.06.019.

Kabuth, A., Dahmke, A., Beyer, C., Bilke, L., Dethlefsen, F., Dietrich, P., Duttmann, R., Ebert, M., Feeser, V., Görke, U.-J., Köber, R., Rabbel, W., Schanz, T., Schäfer, D., Würdemann, H., Bauer, S., 2017. Energy storage in the geological subsurface: dimensioning, risk analysis and spatial planning: the ANGUS+ project. Environ. Earth Sci. 76, 23. https://doi.org/10.1007/s12665-016-6319-5.

Kaye, G.W.C., Laby, T.H., 2016. 3.5. Critical constants and second virial coefficients of gases. In: Tables of Physical and Chemical Constants, 16th edn. Kaye & Laby Online. www.kayelaby.npl.co.uk.

Klein, E., De Lucia, M., Kempka, T., Kühn, M., 2013. Evaluation of long-term mineral trapping at the Ketzin pilot site for CO2 storage: An integrative approach using geochemical modelling and reservoir simulation. Int. J. Greenh. Gas Control 19, 720–730. https://doi.org/10.1016/j.ijggc.2013.05.014.

Klimchouk, A., 1996. The dissolution and conversion of gypsum and anhydrite. Int. J. Speleol. 25, 21–36. https://doi.org/10.5038/1827-806X.25.3.2.

Kolditz, O., Bauer, S., 2004. A process-oriented approach to computing multi-field problems in porous media. J. Hydroinf. 6, 225–244.

Kolditz, O., Bauer, S., Bilke, L., Böttcher, N., Delfs, J.O., Fischer, T., Görke, U.J., Kalbacher, T., Kosakowski, G., McDermott, C.I., Park, C.H., Radu, F., Rink, K., Shao, H., Shao, H.B., Sun, F., Sun, Y.Y., Singh, A.K., Taron, J., Walther, M., Wang, W., Watanabe, N., Wu, Y., Xie, M., Xu, W., Zehner, B., 2012. OpenGeoSys: an open-source initiative for numerical simulation of thermo-hydro-mechanical/chemical (THM/C) processes in porous media. Environ. Earth Sci 67, 589–599. https://doi.org/10.1007/s12665-012-1546-x.

Kushnir, R., Ullmann, A., Dayan, A., 2012. Thermodynamic and hydrodynamic response of compressed air energy storage reservoirs: a review. Rev. Chem. Eng. 28, 123–148. https://doi.org/10.1515/revce-2012-0006.

Lasaga, A.C., 1998. Kinetic Theory In the Earth Sciences. Princeton University Press, Princeton.

Lemmon, E.W., Jacobsen, R.T., Penoncello, S.G., Firend, D.G., 2000. Thermodynamic properties of air and mixtures of nitrogen, argon, and oxygen from 60 to 2000K at pressures to 2000MPa. J. Phys. Chem. Ref. Data 29, 331–385. https://doi.org/10.1063/1.1285884.

Li, D., Bauer, S., Benisch, K., Graupner, B., Beyer, C., 2014. OpenGeoSys-ChemApp: A

coupled simulator for reactive transport in multiphase systems and application to CO2 storage formation in Northern Germany. Acta Geotech 9, 67–79. https://doi.org/10.1007/s11440-013-0234-7.
Li, D., Beyer, C., Bauer, S., 2018. A unified phase equilibrium model for hydrogen solubility and solution density. Int. J. Hydrogen Energy 43, 512–529. https://doi.org/10.1016/j.ijhydene.2017.07.228.
Lowson, R.T., 1982. Aqueous Oxidation of Pyrite by Molecular Oxygen. Chem. Rev. 82, 461–497. https://doi.org/10.1021/cr00051a001.
Mitiku, A.B., Bauer, S., 2013. Optimal use of a dome-shaped anticline structure for CO2 storage: a case study in the North German sedimentary basin. Environ. Earth Sci. 70, 3661–3673. https://doi.org/10.1007/s12665-013-2580-z.
Mitiku, A.B., Li, D., Bauer, S., Beyer, C., 2013. Geochemical modelling of CO2–water–rock interactions in a potential storage formation of the North German sedimentary basin. Appl. Geochem. 36, 168–186. https://doi.org/10.1016/j.apgeochem.2013.06.008.
Moog, H.C., Hagemann, S., 2004. Thermodynamische Modellierung hochsalinarer Lösungen: Gewinnung von Daten für Fe(II), Fe(III) und S(-II) und Entwick - lung eines Programms zur Modellierung des reaktiven Stofftransports im Nahfeld eines Endlagers. Gesellschaft für Anlagen- und Reaktorsicherheit (GRS) mbH.
Nordstrom, D.K., 1982. Aqueous pyrite oxidation and the consequent formation of secondary iron minerals. In: Acid Sulfate Weathering, SSSA Special Publication SV - 10. Soil Science Society of America, Madison, WI, pp. 37–56. https://doi.org/10.2136/sssaspecpub10.c3.
Nordstrom, D.K., Blowes, D.W., Ptacek, C.J., 2015. Hydrogeochemistry and microbiology of mine drainage: An update. Appl. Geochem. 57, 3–16. https://doi.org/10.1016/j.apgeochem.2015.02.008.
Oldenburg, C.M., Pan, L., 2013a. Porous Media Compressed-Air Energy Storage (PM-CAES): Theory and Simulation of the Coupled Wellbore-Reservoir System. Transport Porous Media 97, 201–221. https://doi.org/10.1007/s11242-012-0118-6.
Oldenburg, C.M., Pan, L., 2013b. Utilization of CO2 as cushion gas for porous media compressed air energy storage. Greenh. Gases Sci. Technol. 3, 124–135. https://doi.org/10.1002/ghg.1332.
Palandri, J.L., Kharaka, Y.K., 2004. A compilation of rate parameters of water-mineral interaction kinetics for application to geochemical modeling. USGS Open File Rep 1068, 71. 2004. https://doi.org/10.1098/rspb.2004.2754.
Parkhurst, D.L., Appelo, C.A.J., 2013. Description of input and examples for PHREEQC version 3–A computer program for speciation, batch-reaction, one-dimensional transport, and inverse geochemical calculations. book 6. Techniques and Methods A43 497 p., available only at. http://pubs.usgs.gov/tm/06/a43.
Pearce, J.K., Dawson, G.K.W., Law, A.C.K., Biddle, D., Golding, S.D., 2016a. Reactivity of micas and cap-rock in wet supercritical CO2with SO2and O2at CO2storage conditions. Appl. Geochem. 72, 59–76. https://doi.org/10.1016/j.apgeochem.2016.06.010.
Pearce, J.K., Golab, A., Dawson, G.K.W., Knuefing, L., Goodwin, C., Golding, S.D., 2016b. Mineralogical controls on porosity and water chemistry during O2-SO2-CO2reaction of CO2storage reservoir and cap-rock core. Appl. Geochem. 75, 152–168. https://doi.org/10.1016/j.apgeochem.2016.11.002.
Pei, P., Korom, S.F., Ling, K., He, J., Gil, A., 2015. Thermodynamic impact of aquifer permeability on the performance of a compressed air energy storage plant. Energy Convers. Manag. 97, 340–350. https://doi.org/10.1016/j.enconman.2015.03.072.
Pérez-López, R., Cama, J., Miguel Nieto, J., Ayora, C., Saaltink, M.W., 2009. Attenuation of pyrite oxidation with a fly ash pre-barrier: Reactive transport modelling of column experiments. Appl. Geochem. 24, 1712–1723. https://doi.org/10.1016/j.apgeochem.2009.05.001.
Pfeiffer, W.T., al Hagrey, S.A., Köhn, D., Rabbel, W., Bauer, S., 2016a. Porous media hydrogen storage at a synthetic, heterogeneous field site: numerical simulation of storage operation and geophysical monitoring. Environ. Earth Sci. 75, 1177. https://doi.org/10.1007/s12665-016-5958-x.
Pfeiffer, W.T., Bauer, S., 2015. Subsurface porous media hydrogen storage – scenario development and simulation. Energy Procedia 76, 565–572. https://doi.org/10.1016/j.egypro.2015.07.872.
Pfeiffer, W.T., Beyer, C., Bauer, S., 2017. Hydrogen storage in a heterogeneous sandstone formation: dimensioning and induced hydraulic effects. Pet. Geosci. petgeo2016-050. . https://doi.org/10.1144/petgeo2016-050.
Pfeiffer, W.T., Graupner, B., Bauer, S., 2016b. The coupled non-isothermal, multiphase-multicomponent flow and reactive transport simulator OpenGeoSys–ECLIPSE for porous media gas storage. Environ. Earth Sci. 75, 1347. https://doi.org/10.1007/s12665-016-6168-2.
Pitzer, K.S., 1973. Thermodynamics of electrolytes. I. Theoretical basis and general equations. J. Phys. Chem. 77, 268–277. https://doi.org/10.1021/j100621a026.
Schlumberger, 2016. Eclipse reservoir simulation software v2016.1 – Technical Description Manual. Schlumberger Ltd.
Shiers, D.W., Blight, K.R., Ralph, D.E., 2005. Sodium sulphate and sodium chloride effects on batch culture of iron oxidising bacteria. Hydrometallurgy 80, 75–82. https://doi.org/10.1016/j.hydromet.2005.07.001.
Singer, P.C., Stumm, W., 1970. Acidic Mine Drainage: The Rate-Determining Step. Science 84 167, 1121–1123. https://doi.org/10.1126/science.167.3921.1121.
Sorknæs, P., Mæng, H., Weiss, T., Andersen, A.N., 2013. stoRE Project - Facilitating energy storage to allow high penetration of intermittent renewable energy: Overview of current status and future development scenarios of the electricity system in Denmark – allowing integration of large quantities of wind pow.
Sternberg, A., Bardow, A., 2015. Power-to-What? ? Environmental assessment of energy storage systems. Energy Environ. Sci. 8, 389–400. https://doi.org/10.1039/C4EE03051F.
Succar, S., Williams, R., 2008. Compressed Air Energy Storage : Theory , Resources , And Applications For Wind Power. Princeton University, Energy Analysis Group.
Taylor, P., Evangelou, V.P.B., Zhang, Y.L., 2009. Critical reviews in environmental science and technology a review : pyrite oxidation mechanisms and acid mine drainage prevention a review : pyrite oxidation mechanisms and acid mine drainage prevention. Crit. Rev. Environ. Sci. Technol. 37–41.
The HYDROdynamics Group LCC, 2011. Iowa Stored Energy Plant Agency Compressed-Air Energy Storage Project : FINAL PROJECT REPORT- DALLAS CENTER MT . SIMON STRUCTURE CAES SYSTEM PERFORMANCE ANALYSIS prepared for . Iowa Storage Energy Plant Agency.
The HYDROdynamics Group LCC, 2005. Iowa Stored Energy Plant Agency Compressed-Air Energy Storage Project : COMPRESSED-AIR ENERGY STORAGE HIGH LEVEL RESERVOIR SCREENING EVALUATION IN IOWA prepared for . Electricity and Air Storage Enterprises Houston, Texas.
Wang, B., Bauer, S., 2017a. Compressed air energy storage in porous formations: a feasibility and deliverability study. Petrol. Geosci. 23, 306–314. https://doi.org/10.1144/petgeo2016-049.
Wang, B., Bauer, S., 2017b. Pressure response of large-scale compressed air energy storage in porous formations. Energy Procedia 125, 588–595. https://doi.org/10.1016/j.egypro.2017.08.205.
Wei, N., Li, X., Wang, Y., Zhu, Q., Liu, S., Liu, N., Su, X., 2015. Geochemical impact of aquifer storage for impure CO2 containing O2 and N2: Tongliao field experiment. Appl. Energy 145, 198–210. https://doi.org/10.1016/j.apenergy.2015.01.017.
White, A.F., Peterson, M.L., 1990. Chemical Modeling of Aqueous Systems II, Chemical Modeling of Aqueous Systems II. In: ACS Symposium Series. American Chemical Society, Washington, DC. https://doi.org/10.1021/bk-1990-0416.
Williamson, M.A., Rimstidt, J.D., 1994. The kinetics and electrochemical rate-determining step of aqueous pyrite oxidation. Geochem. Cosmochim. Acta 58, 5443–5454. https://doi.org/10.1016/0016-7037(94)90241-0.
Xie, M., Bauer, S., Kolditz, O., Nowak, T., Shao, H., 2006. Numerical simulation of reactive processes in an experiment with partially saturated bentonite. J. Contam. Hydrol. 83, 122–147. https://doi.org/https://doi.org/10.1016/j.jconhyd.2005.11.003.
Xu, T., Kharaka, Y.K., Doughty, C., Freifeld, B.M., Daley, T.M., 2010. Reactive transport modeling to study changes in water chemistry induced by CO2 injection at the Frio-I Brine Pilot. Chem. Geol. 271, 153–164. https://doi.org/10.1016/j.chemgeo.2010.01.006.
Zabetakis, M.G., 1964. Flammability characteristics of combustible gases and vapors. https://doi.org/10.2172/7328370.
Zerai, B., Saylor, B.Z., Matisoff, G., 2006. Computer simulation of CO2 trapped through mineral precipitation in the Rose Run Sandstone, Ohio. Appl. Geochem. 21, 223–240. https://doi.org/10.1016/j.apgeochem.2005.11.002.
Zhang, W., Li, Y., Xu, T., Cheng, H., Zheng, Y., Xiong, P., 2009. Long-term variations of CO2 trapped in different mechanisms in deep saline formations: A case study of the Songliao Basin, China. Int. J. Greenh. Gas Control 3, 161–180. https://doi.org/10.1016/j.ijggc.2008.07.007.
Zolotov, M.Y., Shock, E.L., 2005. Formation of jarosite-bearing deposits through aqueous oxidation of pyrite at Meridiani Planum, Mars. Geophys. Res. Lett. 32, 1–5. https://doi.org/10.1029/2005GL024253.